nature neuroscience

Molecular interrogation of hypothalamic organization reveals distinct dopamine neuronal subtypes

Roman A Romanov[1,18], Amit Zeisel[2,18], Joanne Bakker[3], Fatima Girach[1], Arash Hellysaz[3], Raju Tomer[4], Alán Alpár[5,6], Jan Mulder[7], Frédéric Clotman[8], Erik Keimpema[1], Brian Hsueh[4], Ailey K Crow[4], Henrik Martens[9], Christian Schwindling[10], Daniela Calvigioni[1,3], Jaideep S Bains[11], Zoltán Máté[12], Gábor Szabó[12], Yuchio Yanagawa[13], Ming-Dong Zhang[3], Andre Rendeiro[14], Matthias Farlik[14], Mathias Uhlén[15], Peer Wulff[16], Christoph Bock[14], Christian Broberger[3], Karl Deisseroth[4], Tomas Hökfelt[3], Sten Linnarsson[2], Tamas L Horvath[17,19] & Tibor Harkany[1,3,19]

The hypothalamus contains the highest diversity of neurons in the brain. Many of these neurons can co-release neurotransmitters and neuropeptides in a use-dependent manner. Investigators have hitherto relied on candidate protein-based tools to correlate behavioral, endocrine and gender traits with hypothalamic neuron identity. Here we map neuronal identities in the hypothalamus by single-cell RNA sequencing. We distinguished 62 neuronal subtypes producing glutamatergic, dopaminergic or GABAergic markers for synaptic neurotransmission and harboring the ability to engage in task-dependent neurotransmitter switching. We identified dopamine neurons that uniquely coexpress the *Onecut3* and *Nmur2* genes, and placed these in the periventricular nucleus with many synaptic afferents arising from neuromedin S$^+$ neurons of the suprachiasmatic nucleus. These neuroendocrine dopamine cells may contribute to the dopaminergic inhibition of prolactin secretion diurnally, as their neuromedin S$^+$ inputs originate from neurons expressing *Per2* and *Per3* and their tyrosine hydroxylase phosphorylation is regulated in a circadian fashion. Overall, our catalog of neuronal subclasses provides new understanding of hypothalamic organization and function.

In contrast to the cerebral cortex and cerebellum, the hypothalamus lacks distinct layering or other stringent anatomical, repetitive organizational principles. Since the discovery of vasopressin and oxytocin[1] and of the releasing and release-inhibiting factors[2] in the magno- and parvocellular hypothalamic systems, respectively, neuropeptides have been a basis for defining and understanding hypothalamic organization and functionality. Coordination of activity within the hypothalamic circuitry, including its functionally heterogeneous subnetworks composed of molecularly diverse and spatially segregated neuroendocrine neurons[3], is vital to maintaining adaptive responsiveness and homeostatic control of the body.

As an example of functional complexity within a circumscribed brain volume, eight subdivisions are distinguishable within the paraventricular nucleus (PVN) alone[4]. These contain both magno- and parvocellular neuroendocrine secretory motor neurons, as well as parvocellular neurons projecting to the brainstem and spinal cord. Alternatively, a continuum of dopamine neurons in the hypothalamus (A11, A12, A14 and A15 groups), centered around the arcuate nucleus (Arc) and adjacent hypothalamic and extrahypothalamic brain areas (for example, preoptic region rostrally, zona incerta in dorsal extension and midbrain caudally; A8–11 and A13), is arranged such that spatial segregation encodes function determination[5,6]. However, the degree of molecular diversity among dopamine neurons remains unknown.

Here we used single-cell RNA-seq in dissociated neurons from a central column of the mouse hypothalamus to generate a comprehensive catalog of neuronal identities. We reveal 62 neuronal subclasses in the conglomerate of hypothalamic nuclei sampled, many of which cluster uniquely through novel identity marks. We used a multiparametric approach aided by transgenic technologies to define four subtypes of dopaminergic neurons, with one selectively expressing onecut-3 (*Onecut3*) and neuromedin U receptor 2 (*Nmur2*). We then

[1]Department of Molecular Neurosciences, Center for Brain Research, Medical University of Vienna, Vienna, Austria. [2]Division of Molecular Neurobiology, Department of Medical Biochemistry and Biophysics, Karolinska Institutet, Stockholm, Sweden. [3]Department of Neuroscience, Karolinska Institutet, Stockholm, Sweden. [4]Department of Bioengineering & CNC Program, Stanford University, Stanford, California, USA. [5]MTA-SE NAP Research Group of Experimental Neuroanatomy and Developmental Biology, Hungarian Academy of Sciences, Budapest, Hungary. [6]Department of Anatomy, Semmelweis University, Budapest, Hungary. [7]Science for Life Laboratories, Department of Neuroscience, Karolinska Institutet, Stockholm, Sweden. [8]Laboratory of Neural Differentiation, Institute of Neuroscience, Université Catholique de Louvain, Brussels, Belgium. [9]Synaptic Systems GmbH, Göttingen, Germany. [10]Microscopy Labs Munich, Global Sales Support-Life Sciences, Carl Zeiss Microscopy GmbH, Munich, Germany. [11]The Hotchkiss Brain Institute, University of Calgary, Calgary, Alberta, Canada. [12]Institute of Experimental Medicine, Hungarian Academy of Sciences, Budapest, Hungary. [13]Department of Genetic and Behavioral Neuroscience, Gunma University Graduate School of Medicine, Maebashi, Japan. [14]CeMM Research Center for Molecular Medicine of the Austrian Academy of Sciences, Vienna, Austria. [15]Science for Life Laboratory, Albanova University Center, Royal Institute of Technology, Stockholm, Sweden. [16]Institute of Physiology, Christian Albrechts University, Kiel, Germany. [17]Program in Integrative Cell Signaling and Neurobiology of Metabolism, Section of Comparative Medicine, Yale University School of Medicine, New Haven, Connecticut, USA. [18]These authors contributed equally to this work. [19]These authors jointly directed this work. Correspondence should be addressed to T.L.H. (tamas.horvath@yale.edu) or T. Harkany (tibor.harkany@meduniwien.ac.at).

Received 27 June; accepted 18 November; published online 19 December 2016; doi:10.1038/nn.4462

employed circuit mapping in intact tissues in combination with Ca^{2+} imaging to show that a neuromedin S–neuromedin U receptor 2 axis exists between glutamatergic suprachiasmatic nucleus (SCN) neurons and periventricular dopamine cells, thus resolving the long-standing debate about the identity of neurons and neuropeptide systems integrating dopamine output into the circadian circuitry[7,8].

RESULTS

Diversity of cell types in the mouse hypothalamus

Single-cell RNA-seq data were obtained from 3,131 cells dissociated from a central column of the medial-ventral diencephalon (**Fig. 1a**), including in its rostrocaudal extent the posterior part of the preoptic area (bregma −0.5 mm) and in the caudal direction the Arc (bregma −2.3 mm). We relied on a divisive biclustering method using the BackSpinV2 algorithm[9], which sorts cells into clusters of closest neighbors. Using lineage-specific known and new protogenes (see "Level 1 analysis," Online Methods), this procedure allowed us to distinguish seven main cell types (**Fig. 1a**,**b**). To determine neuronal subclass diversity, we performed second-level clustering on hypothalamic neurons (**Fig. 1c**). The analysis of 898 neurons classified these cells into 62 clusters with high-quality content (as assessed by donors per cluster, detected genes per cell, total molecules detected; **Supplementary Fig. 1a–c**), prominently featuring neuropeptides (**Fig. 1d**) and enzymes involved in neurotransmitter turnover.

Cell state changes and neuronal identity

The mammalian hypothalamus exhibits significant gender distinctions, including the number and content of neuronal subtypes[10,11]. Previous genome-wide profiling studies aimed to resolve gender-related traits and linked those to specific behaviors[12,13]. Even though we minimized the effects of sexual dimorphism by using mice before they reached the age of sexual maturation (postnatal days 21 ± 7), we used the molecular resolution of single-cell RNA-seq to test whether sex determination exists in neuronal cohorts making up the mouse hypothalamus. Hierarchical clustering did not reveal major differences in neuronal heterogeneity between female and male hypothalamic counterparts (**Supplementary Fig. 2a**). This allowed us to pool data from both sexes. Nevertheless, several neuronal clusters were dominated by neurons from male (for example, cluster 55) or female (cluster 6) subjects, suggesting, but not definitively establishing, gender-specific coding (**Supplementary Fig. 2a**).

Neuronal networks in the mammalian hypothalamus can change the predominance of their main fast neurotransmitter and/or neuropeptide signaling system within hours upon metabolic challenge[14–16]. For example, glutamate-to-GABA switches can occur as a result of the reorganization of synaptic circuits upon feeding[16,17]. The ability of neurons to harbor mRNAs encoding enzymes and transporters indispensable for the production or release of multiple neurotransmitters may indicate an alternative mechanism of neuronal state switches. Therefore, we asked whether acute stress by peripheral paraformaldehyde injection and sampling 6 h later[18] would affect cluster dynamics. Our unbiased clustering rejected any change to cluster assignment, thus arguing against the rapid generation of novel neuronal subtypes upon stress (**Supplementary Fig. 2b**).

Neuronal heterogeneity in the hypothalamus

Classical criteria on neuronal diversity in the hypothalamus use neuropeptides[19], and, less frequently, fast neurotransmitters as identifying marks for functionally specialized neuronal pools[20]. However, there is no consensus on, or direct correlation between, neurotransmitter and neuropeptide expression patterns.

Here, we first used *t*-dependent stochastic neighbor embedding (tSNE) to visualize our multidimensional data set (**Fig. 1d** and **Supplementary Figs. 3** and **4**). By relying on a combination of neuropeptides (**Supplementary Table 1**), enzymes and neurotransmitter transporters that rate-limit synaptic signaling, we provide an unbiased list of neuropeptides and/or hormones that define neuronal subtypes by forming spatially segregated cell clusters (**Fig. 1d**). Proopiomelanocortin (*Pomc* gene) represents a clustering example. In contrast, the gene encoding corticotropin-releasing hormone (*Crh*) was not restricted to a neuronal subset. Instead, our analysis suggests that many hypothalamic neurons, including both GABA and glutamate phenotypes (**Supplementary Fig. 5a–d**), can produce and secrete *Crh* under certain metabolic conditions (**Fig. 1d** and **Supplementary Fig. 5**). Thus, single-cell RNA-seq allowed us to distinguish transcript patterns that encode homogeneity or, conversely, molecular differences.

Hierarchical clustering reveals neurotransmitter–neuropeptide relationships

Next we filtered our single-cell RNA-seq data[9] to distinguish stable neuronal clusters whose borders and marker gene homogeneities were manually confirmed (**Supplementary Table 2**). We produced a hierarchical dendrogram (**Fig. 2a**) that segregated neurotransmitter and neuropeptide-containing cells into subclasses. Junction points and their specificities are listed in **Supplementary Table 3**. Based on the most abundant gene marks ('top five filtering'; **Supplementary Table 3**), we introduce a specific terminology that reflects differential gene expression related to neurotransmitters, neuropeptides and function determination (for example, circadian rhythm) (**Fig. 2a**). Neurotransmitter identities included glutamatergic (clusters 1–7 and 30–62), dopaminergic (8–11) and GABAergic (12–29) cells. Notably, both the glutamate mark *Slc17a6* and the dopamine mark *Th* were of low abundance in oxytocin (*Oxt*) and vasopressin (*Avp*)-containing neuroendocrine clusters (cluster 1–7; **Fig. 2b**), suggesting that these cells under normal conditions may primarily act via their respective hormones. The significance of *Th* and tyrosine hydroxylase protein in these neurons remains unclear because they appear to lack the gene for aromatic amino acid decarboxylase (AADC; for *Ddc* and other genes see **Supplementary Table 2** and http://linnarssonlab.org/hypothalamus/), the enzyme needed for dopamine synthesis. Subsequent differential mRNA expression analysis subdivided *Oxt* and *Avp* neurosecretory cells, which project to the posterior lobe of the pituitary[4], into three and four subtypes, respectively (**Supplementary Table 3**).

In comparison, non-magnocellular cells present a more heterogeneous picture. They can be separated into GABAergic (*Gad1*, *Gad2* and *Slc32a1*) and glutamatergic (*Slc17a6*) subtypes[20]. GABA neurons varied in their expression levels of *Gad1* and *Gad2*, encoding GAD67 and GAD65, respectively (**Fig. 2b**). This was particularly notable for cluster 8–11 cells (with low *Gad1* and high *Gad2*), which also harbored *Th*, *Slc18a2* (vesicular monoamine transporter 2, VMAT2) and, in some cases, *Slc6a3* (encoding dopamine transporter 1, DAT), qualifying them as dopamine neurons and suggesting the existence of dual dopamine/GABA neurotransmitter phenotypes (**Fig. 3a**; see also ref. 21). Our hierarchical clustering approach also separated 33 clusters of mostly glutamatergic modalities (clusters 28–62). Some of these neuronal subtypes also contained *Gad1* or *Gad2* and/or *Slc32a1* mRNAs. For further validation we performed a sequencing study using another technique, Drop-seq[22]. In 220 neurons, we recaptured subsets of GABA, glutamate and dopamine cells that contained genes for alternative neurotransmission (**Fig. 3b**). Notably, and despite the different proportion of GABAergic, glutamatergic and dopaminergic

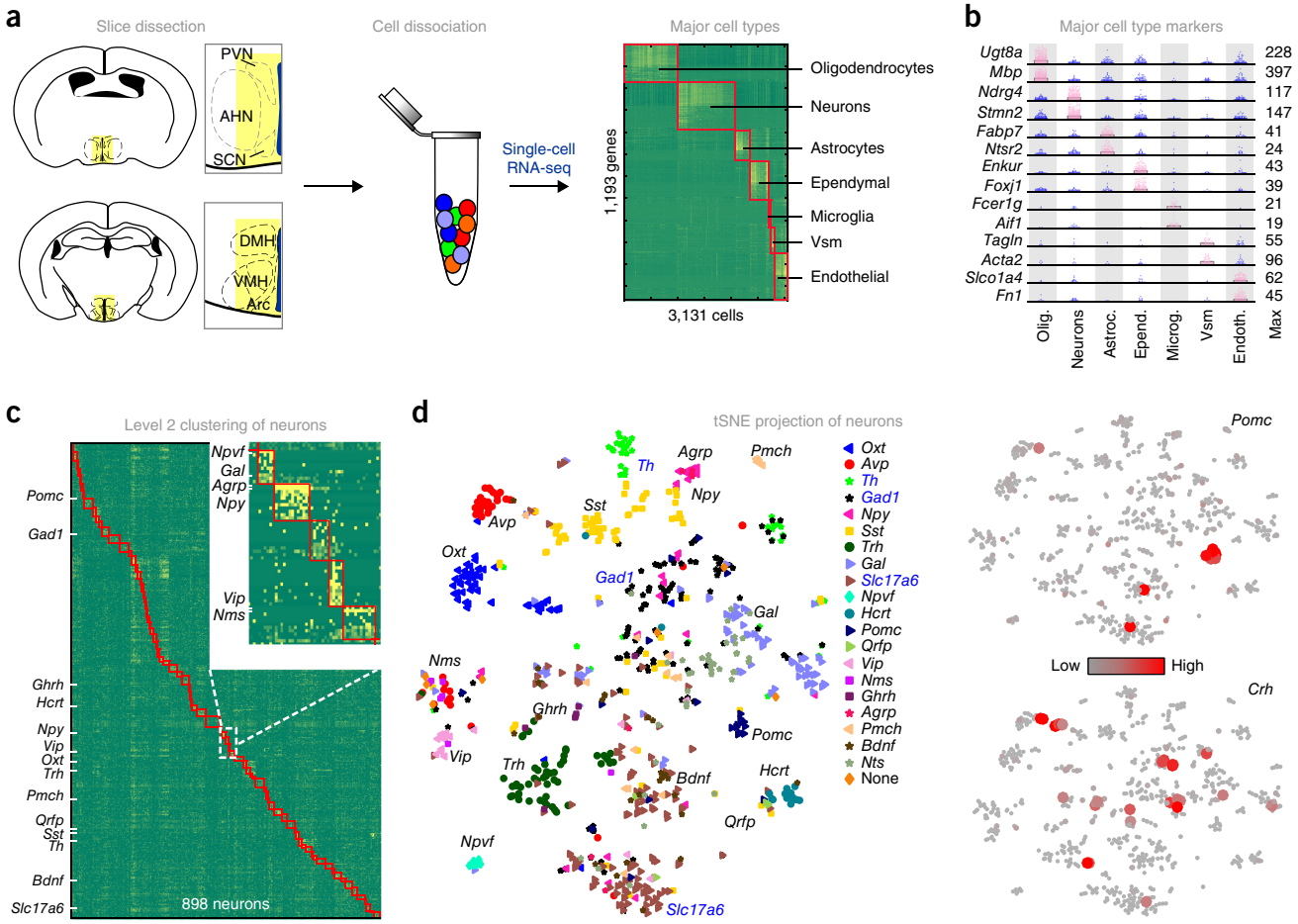

Figure 1 Cell-type diversity in the mouse hypothalamus. (**a**) Workflow diagram for indiscriminately obtaining intact single cells from the juvenile mouse hypothalamus and analyzing them without selection. A central vertical column spanning the preoptic area and arcuate nucleus in its rostrocaudal extent (yellow shading) was dissected, enzymatically dissociated and processed for single-cell RNA-seq. Molecule counts from 3,131 cells were first clustered to define main cell types. Heat map shows blocks of genes enriched in each cell type. (**b**) mRNA transcripts specifying each of the seven major cell types. Dot density plots depict means (bars) and individual values (circles). mRNA expression of selected known and novel markers. A marker pair (pink) is shown for each class, including a generally accepted and a lesser-known gene. Olig., oligodendrocytes; Astroc., astrocytes; Epend., ependymal cells; Microg., microglia; Vsm, vascular and smooth muscle lineage; Endoth., endothelial cells. (**c**) Clustering of 898 neurons reveals molecular diversity. Heat map shows clustering results, with blocks of clusters aligned along the diagonal axis and boxed in red. Gene symbols in inset denote subtype-specific neuropeptides and hormones. (**d**) Left: visualization of hypothalamic neuron subtypes on a two-dimensional map using tSNE (1,194 genes, perplexity = 5, 200 principal components; see also **Supplementary Figs. 3** and **4**). Neurons were color-coded by highest expression of well-known, cluster-defining hypothalamic markers. Top right: *Pomc* mRNA expression is an example of phenotypic clustering on the same tSNE plot. Bottom right: in contrast, *Crh* is heterogeneously distributed on the tSNE scaffold, precluding its use to typify neurons. *Agrp*, agouti-related peptide; *Avp*, arginine-vasopressin; *Bdnf*, brain-derived neurotrophic factor; *Gad1*, glutamate decarboxylase 1; *Gal*, galanin; *Ghrh*, gonadotropin-releasing hormone; *Hcrt*, hypocretin; *Nms*, neuromedin S; *Npvf*, neuropeptide VF precursor; *Npy*, neuropeptide Y; *Oxt*, oxytocin; *Pmch*, promelanin-concentrating hormone; *Pomc*, proopiomelanocortin; *Qrfp*, pyroglutamylated RF amide peptide; *Slc17a6*, vesicular glutamate transporter 2; *Sst*, somatostatin; *Th*, tyrosine hydroxylase; *Trh*, thyrotropin-releasing hormone; *Vip*, vasoactive intestinal polypeptide.

cells in the pool of neurons sampled by Drop-seq, we found strikingly similar numbers of cells that exhibited the ability of dual neurotransmission (**Fig. 3b**). Lastly, we employed multiple immunofluorescence labeling to show the coexistence of VGLUT2 and GAD67 proteins in nerve endings at the median eminence (**Fig. 3c**,**d**). Likewise, we determined that even very low mRNA copy numbers can be biologically meaningful by showing the coexistence of vasopressin and VGLUT2 (**Fig. 3e**, left) and GAD67 (**Fig. 3e**, right). Quantitatively, we confirmed by three-dimensional laser-scanning microscopy that 36 terminals contained both VGLUT2 and GAD67 out of 790 VGLUT2$^+$ (~4.6%) or 1,221 GAD67$^+$ (~3.0%) nerve endings located in identical surface areas in the median eminence. In sum, these data reinforce our conclusion that hypothalamic neurons might either co-release neurotransmitters, segregate them to subsets of synapses or switch between modes of neurotransmission in response to specific inputs, thus allowing fast output modulation[16,17].

Owing to the hypothesis that neuropeptides can modulate the action of fast neurotransmitters, as well as being signal-competent on their own[23], we established neurotransmitter–neuropeptide relationships. To this end, we determined the total number of mRNA molecules for the top 52 known neuropeptide hits (**Supplementary Table 1**), which ranged from 0 to >30,000 per neuronal subtype. *Oxt* and *Avp* neurons frequently expressed the *Pdyn* gene (encoding prodynorphin) (**Fig. 4**). Dopamine neurons chiefly coexpressed the genes for tachykinin 1 (*Tac1*) and nociceptin (*Pnoc*). For GABA neurons, clusters 12–17 (GABA1–6 subtypes) were relatively sparse

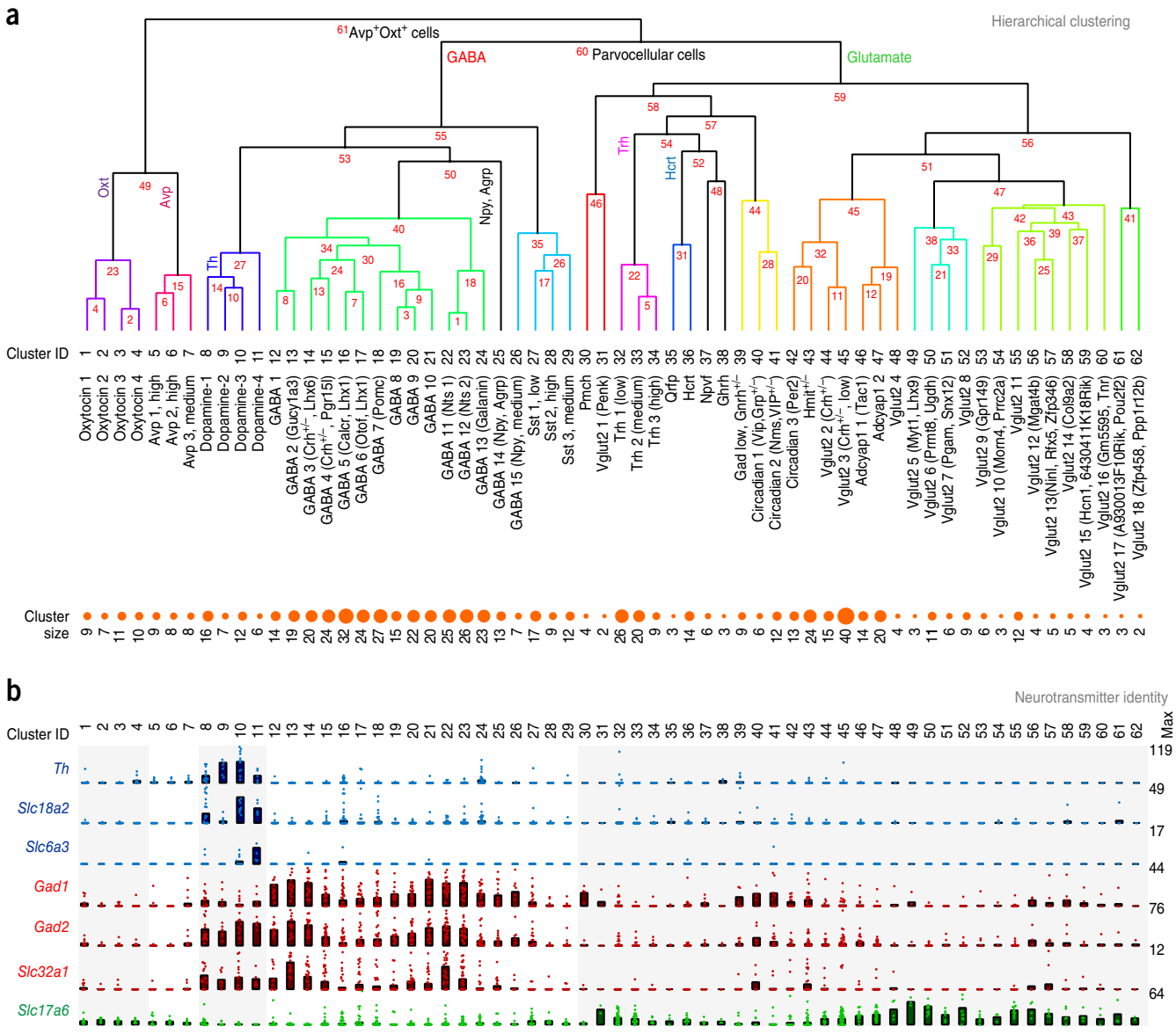

Figure 2 Hierarchical clustering of hypothalamic neuron subtypes. (**a**) Classification of 62 neuronal subtypes as defined by unique molecular fingerprints (i.e., top five genes). Numbers in red indicate divergence points defined by the BackSpinV2 algorithm. We adopted a terminology that relies on neurotransmitter and subtype-specific gene sets. Cluster size indicates the number of neurons assigned to a specific subtype. (**b**) Neurotransmitter specificity in each neuronal subtype was defined by their expression of tyrosine hydroxylase (*Th*), vesicular monoamine transporter 2 (*Slc18a2*) and dopamine transporter 1 (*Slc6a3*) for dopaminergic neurons, glutamate decarboxylase 1 and 2 (*Gad1*, *Gad2*) and vesicular GABA transporter (*Slc32a1*) for GABAergic neurons, and vesicular glutamate transporter 2 (*Slc17a6*) for glutamatergic neurons. Note the existence of dual neurotransmitter phenotypes. Dot density plots show mean expression per cluster × percentage of cells (bars), as well as individual values (circles). Numbers to the right indicate the maximum number of molecules for each gene, thus providing ranges from 0 to maximum value. +/– in the cluster names refers to fractional gene expression.

in neuropeptide genes (such genes include *Crh* (clusters 14 and 15) and *Tac2* (clusters 13 and 15)). In contrast, clusters 18–29 were separated by primary gene expression for neuropeptides, including *Pomc* (cluster 18), *Pnoc* (19 and 20), *Tac2* (20–24), *Nts* (22 and 23), *Gal* (24), *Agrp* (25), *Npy* (25 and 26) and *Sst* (27–29) mRNAs (**Fig. 4** and **Supplementary Table 4**). Lastly, glutamatergic neurons showed an apparent variability in their gene expression for neuropeptides, as clusters 33–35 contained *Trh*, *Bdnf* and *Adcyap1* mRNAs whereas clusters 57–62 exhibited only marginal (if any) expression of genes for polypeptides (**Supplementary Table 4**). However, even if clusters were closely placed, their differential expression profiles revealed specificity in individual and/or combinatorial expression of genes: cluster 62–enriched genes included *Zfp458* and *Ppp1r12b*, whereas neurons in cluster 61 were enriched in *Pou2f2* (**Supplementary Fig. 6a** and **Supplementary Tables 2** and **3**). For clusters 22 and 23, we noted the differential expression of the hypocretin (orexin) receptor 1 and 2 genes (*Hcrtr1* and *Hcrtr2*), establishing their molecular divergence (http://linnarssonlab.org/hypothalamus/). Cumulatively, these data advance existing knowledge on the molecular heterogeneity of dopamine, GABA and glutamate neurons in the hypothalamus and allow inferences be made on the positioning, circuit recruitment and signal diversity of specific neuronal subtypes (for subtype-specific markers, see **Supplementary Fig. 6a**).

Molecular validation through new neuropeptide marks

Our single-cell RNA-seq data allowed the identification of many new markers with a high degree of subclass selectivity (**Supplementary Fig. 6a** and **Supplementary Tables 5** and **6**). In addition, we also identified combinations of genes whose coexpression patterns predicted individual subclusters with a high degree of accuracy (for example, *Shf* alone versus *Shf* plus *Sfrp2*, or *Dlx1* alone versus *Dlx1* plus *Zfp865*). Based on the cluster marks used (**Supplementary Figs. 6** and **7a**), we identified two new neuronal subtypes specifically expressing the gene for either pyroglutamylated RF amide peptide (*Qrfp*; **Supplementary Fig. 6b**) or neuropeptide VF (*Npvf*; **Supplementary Fig. 6c**)[24,25]. Accordingly, *Qrfp*- and *Npvf*-expressing hypothalamic neurons were both glutamatergic and segregated into clusters 35 and 37, respectively (**Supplementary Fig. 6b,c**). Moreover, we found that *Qrfp*$^+$ and *Npvf*$^+$ hypothalamic neurons coexpressed the genes for hypocretin (*Hcrt*; **Supplementary Fig. 6b**) and galanin (*Gal*; **Supplementary Fig. 6c**), respectively. Thus, and also considering that both *Qrfp* and *Npvf* qualify as cell identity marks (**Fig. 2a**), we establish these neurons as bona fide excitatory neuropeptidergic subtypes.

Expression-based prediction of a new dopamine neuron subtype

Single-cell RNA-seq of dissociated tissues provides compelling information on the molecular makeup of particular cell lineages and allows hypotheses to be formulated regarding functional divergence, particularly neuronal circuit wiring through, for example, transmitter–receptor relationships. However, the often small cluster size (<10 cells) and the lack of positional information *per se* could render single-cell RNA-seq data liable to false positive outcomes. Therefore, we set out to validate our data by choosing the predicted fourth subtype of dopamine neurons (cluster 11; 'dopamine-4 cells'), which, despite its small sample size (6 neurons), segregated from other dopamine clusters in our predictive model (**Fig. 5a**).

First we compared fractional gene expression (**Fig. 5b**), as well as average amplitude expression (**Supplementary Table 3**) between dopamine subtypes 1–3 versus 4 to reveal whether any gene can be used to hallmark this predicted dopamine subclass. Differentially expressed genes selectively enriched in dopamine-4 cells included those for the transcription factor onecut-3 (*Onecut3*), *Nmur2*, *Nmbr*, *Robo1*, DAT (*Slc6a3*), K$^+$ channels (*Kcnh1*), secretory proteins (*Cadps2*), genes associated with intracellular signaling (*Rabl3*, *Gpn3* and *Plch1*), cytoskeletal dynamics (*Kank4* and *Gprin1*), unannotated genes (*2010001M06Rik*, *A430033K04Rik*) and *Sst* (**Supplementary Table 3**). In turn, these cells lacked neuropeptides that were abundant in other dopamine subclasses, such as *Ghrh1* and *Tac1* (**Fig. 5b**). Most of these cells (~70%) also lacked *Npy2r*, the gene encoding neuropeptide Y receptor Y2. Subsequently, we broadened our specificity testing to all 62 predicted neuronal clusters and found that, unlike *Th* and *Sst*, which were broadly expressed, both *Slc6a3* and *Onecut3* were predominantly restricted to this particular cell population (**Fig. 5c**). Thus, coincident DAT and onecut-3 localization could reveal whether these neurons are spatially segregated from or intermingled with other dopamine cells.

Next we explored the distribution of onecut-3 and DAT in hypothalamic dopamine neurons using a combination of immunohistochemistry (**Fig. 5d**) and mouse genetics, particularly in *Th-GFP* and *Dat1-Cre::ROSA26Sor*$^{CAG\text{-}tdTomato}$ mice, allowing life-long expression profiling (**Supplementary Fig. 7b–d**). Coincident detection of onecut-3 and enzymatically active TH phosphorylated at residue Ser40 (ref. 26) on a *Th-GFP* background revealed that these dopamine neurons populate the periventricular nucleus of the hypothalamus (**Fig. 5d**), with their dendritic trees being primarily oriented vertically

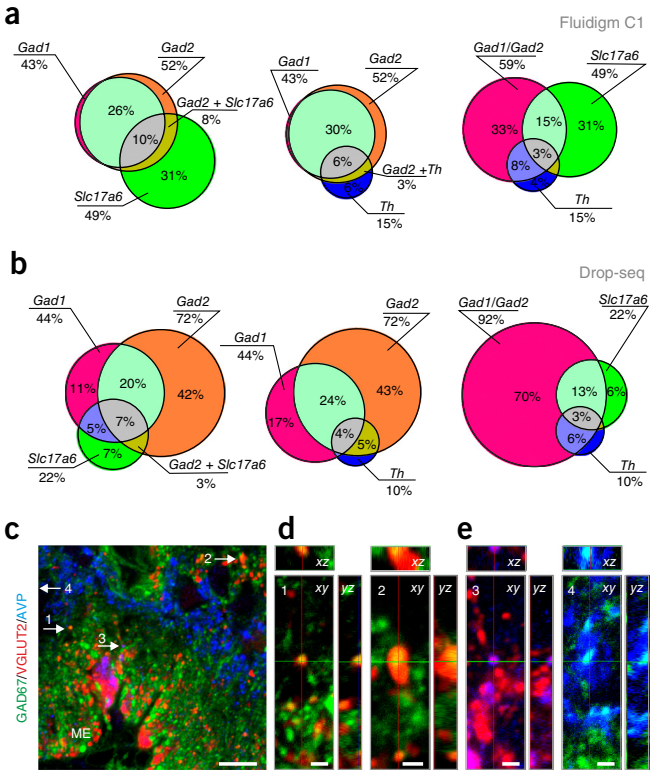

Figure 3 Neurotransmitter phenotypes in hypothalamic neurons. (**a**,**b**) Venn diagrams showing the proportion of dual and triple neuronal phenotypes representing GABA/glutamate (left), GABA/dopamine (middle) and GABA/glutamate/dopamine (right) neurons after Fluidigm C1 (**a**) or Drop-seq (**b**) sequencing. Percentage values indicate the proportion of neurons falling into groups and intersections (dual-phenotype categories). (**c**–**e**) Histochemical validation of neurotransmitter heterogeneity in axon terminals at the median eminence (ME; **c**), showing the coexistence of GAD67 and VGLUT2 (**d**, arrows in **c**), of vasopressin (AVP) and VGLUT2 (**e**, left), and of AVP and GAD67 (**e**, right). Orthogonal image stacks are shown; red, blue and green lines and crosshairs in **d**,**e** are used to show 3D coordinates and define the area of interest. Arrows 1–3 in **c** correspond to numbered insets in **d** and **e**. Arrow 4 points to a position placed outside the image boundary. Scale bars: 10 µm (**c**) and 2 µm (**d**,**e**).

(**Fig. 5e**). By using serial sections (**Fig. 5d**) and reconstructive histochemistry in optically cleared tissues (**Fig. 5f**, **Supplementary Fig. 7e** and **Supplementary Videos 1–3**), we determined that onecut-3$^+$ dopamine neurons formed a cell continuum spanning the SCN–Arc domain with an increasing cell gradient caudally, thus qualifying as A14 dopamine neurons[6,27]. Lightsheet microscopy revealed 474 cells in an adult mouse brain (**Fig. 5f** and **Supplementary Videos 1** and **2**), while conventional neuroanatomy in serial sections projected 500–1,000 cells per brain. Notably, these neurons segregated dorsally from other dopamine cells residing in the Arc (**Fig. 5d**,**f** and **Supplementary Video 2**). Quantifying GFP intensity in these TH$^+$ cells, we found that their GFP signal was significantly ($P < 0.001$) lower than that of other TH$^+$ cell groups (**Supplementary Fig. 7c**), while their phospho-Ser40 levels were distinctly elevated (**Supplementary Fig. 7c**). These data reinforce our single-cell RNA-seq results, which demonstrated low *Th* mRNA copy numbers in dopamine-4 neurons (**Fig. 5c**). Lastly, we studied post-mortem human hypothalami (**Fig. 5g**) and found that a neuronal cohort positioned proximal to the third ventricle possessed a molecular profile of onecut-3 and phospho-Ser40-TH reminiscent of that in mouse, suggesting that our differential classification

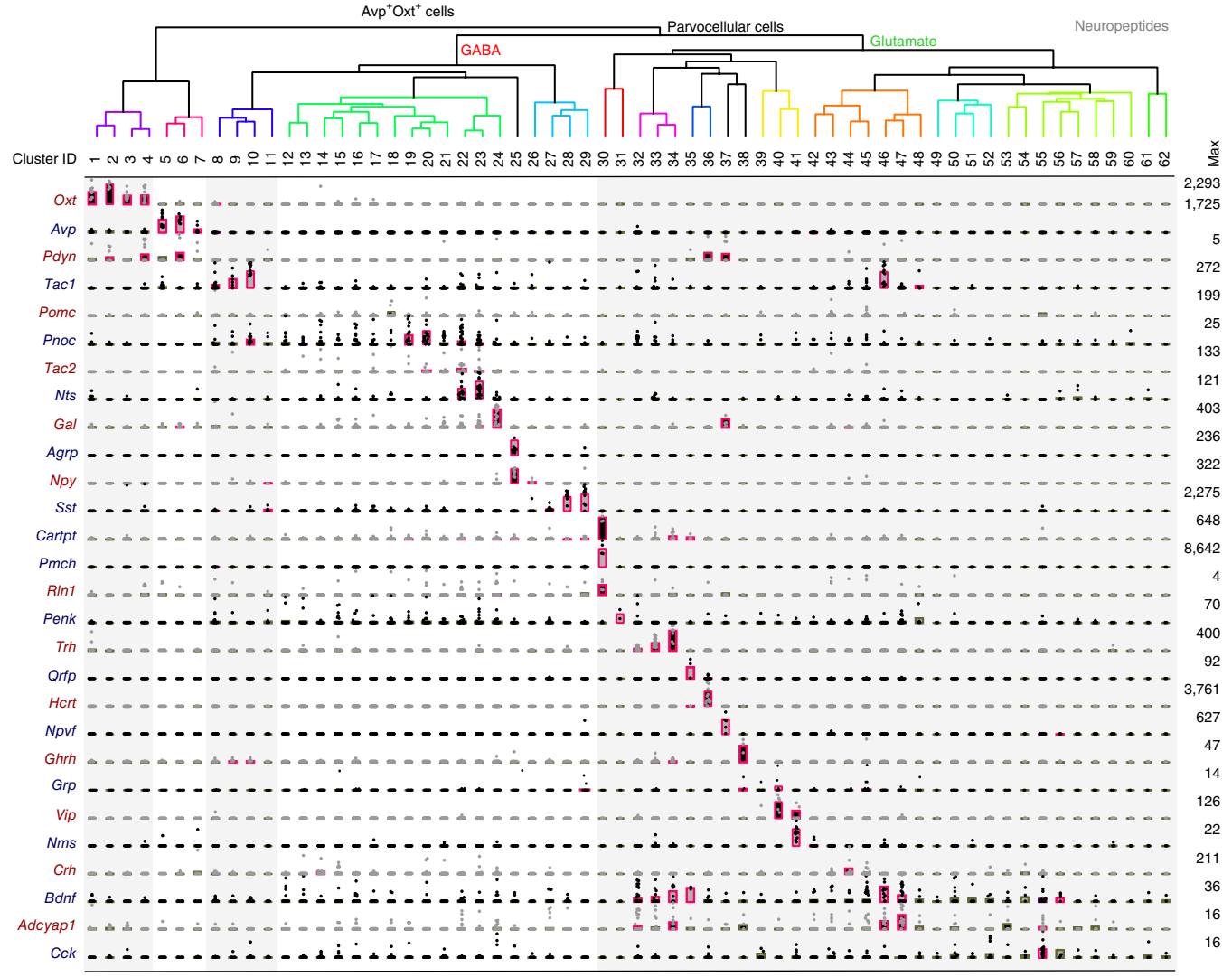

Figure 4 Neuropeptide associations to individual hypothalamic neuronal subtypes. Neuronal subtypes were clustered as in **Figure 2**. Vertical shaded columns denote main neuropeptide mRNA contents per neuronal subclass as in **Figure 2**, including level of statistical significance at $q < 0.05$ (magenta). Dot density plots show mRNA expression levels per cell. *Adcyap1*, adenylate cyclase activating polypeptide 1; *Agrp*, agouti-related peptide; *Avp*, arginine-vasopressin; *Bdnf*, brain-derived neurotrophic factor; *Cartpt*, cocaine and amphetamine regulated transcript prepropeptide; *Cck*, cholecystokinin; *Crh*, corticotropin-releasing hormone; *Gal*, galanin; *Ghrh*, growth hormone-releasing hormone; *Grp*, gastrin-releasing peptide; *Hcrt*, hypocretin; *Nms*, neuromedin S; *Npvf*, neuropeptide VF precursor; *Npy*, neuropeptide Y; *Nts*, neurotensin; *Oxt*, oxytocin; *Pdyn*, prodynorphin; *Penk*, proenkephalin; *Pmch*, promelanin-concentrating hormone; *Pomc*, proopiomelanocortin; *Pnoc*; prepronociceptin; *Qrfp*, pyroglutamylated RF amide peptide; *Rin1*, Ras and Rab interactor 1; *Sst*, somatostatin; *Tac1*, substance P (tachykinin 1); *Tac2*, tachykinin 2; *Trh*, thyrotropin-releasing hormone; *Vip*, vasoactive intestinal polypeptide.

of dopamine neurons may be broadly relevant to defining neuronal diversity in the hypothalamus of various mammals.

Morphological stratification of dopamine neurons in intact brains

We found that dopamine-4 neurons (A14, cluster 11) expressed the gene for DAT (*Slc6a3*; **Fig. 6a**), contrasting with ventrolateral Arc A12 neurons but being in *Slc6a3* expression similar to the dorsomedial A12 group[28]. The latter neuronal pool also contains GAD[21] and is a source of dopamine inhibiting prolactin release[29]. The expression of DAT (**Fig. 6a**) could help A14 neurons, like dorsomedial Arc A12 neurons, to regulate ambient levels of dopamine[30]. The expression of DAT in these cells also allowed us to combine advanced optical imaging and mouse genetics: we used AAV-driven and Cre-dependent GFP expression in *Dat1-Cre* mice to address intrahypothalamic projection sites for dopamine-4 neurons (**Fig. 6b**). GFP distribution revealed ventrally running fine processes with pearl-lace-like appearance, likely axons. Most of these processes detoured around the Arc and coursed laterally, as also suggested by the differential expression of phospho-Ser40-TH in processes putatively originating in A14 dopamine-4 neurons (**Fig. 6c**). Moreover, histochemical detection of TH using CLARITY optimized lightsheet microscopy demonstrated that most TH$^+$ axons leaving the A14 area projected laterally using the supraoptic decussation and upper lateral pathway and terminated outside the hypothalamus, likely in basolateral and central amygdaloid nuclei (**Fig. 6d**, **Supplementary Fig. 7e** and **Supplementary Video 3**). Notably, the median eminence was a site where DAT immunoreactivity accumulated (**Fig. 6e**), including sporadic colocalization with SST in terminal-like specializations (**Fig. 6f**), pinpointing the median

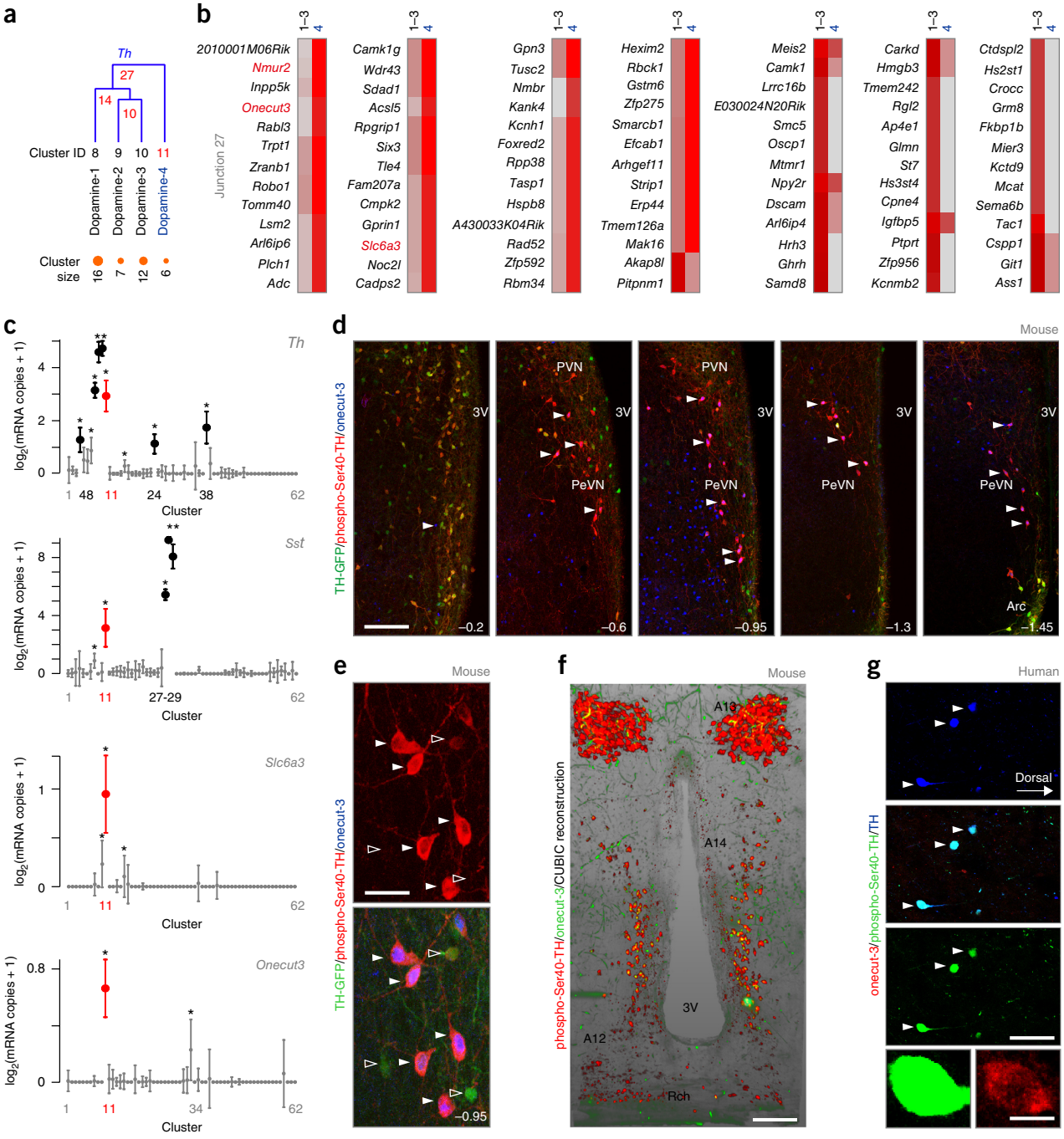

Figure 5 Molecular interrogation of dopamine neurons defines a onecut-3-expressing periventricular subtype. (**a**) Segregation of tyrosine hydroxylase (*Th*)-expressing neurons into 4 subtypes, as defined by their divergent expression of the top five genes (see also **Fig. 2**). Dopamine neuron subclass 4 segregates early from the other subclasses. On the top, numbers in red indicate divergence points (junctions) defined by dendrogram construction. Neuronal cluster sizes (number of cells) are shown below. (**b**) Differential gene expression profile of dopamine neuron subtypes 1–3 (cumulative) versus subtype 4. mRNA transcripts in red, including onecut-3 (*Onecut3*), define subclass identity. Incremental mRNA expression was color coded from gray (no detectable expression) to deep red. (**c**) Selective coexpression (in red) of *Th*, *Slc6a3*, *Onecut3* and *Sst* in the dopamine-4 subclass (cluster 11). Data are presented as 'power 1' error-bar plots. Data exceeding 2 s.e.m. for *Th* and *Sst* in other neuronal clusters are shown in black. $*q < 0.05$ (Wilcoxon rank-sum test corrected for multiple testing). (**d**) Distribution of phospho-Ser40-TH$^+$ and onecut-3$^+$ neurons at select anterior–posterior coordinates (in millimeters relative to bregma) in the hypothalamus of *Th-GFP* reporter mice. Multi-labeled neurons concentrate (arrowheads) in the periventricular hypothalamic nucleus (PeVN). (**e**) High-resolution photomicrograph depicting PeVN dopamine neurons coexpressing phospho-Ser40-TH and onecut-3 (filled arrowheads), with elaborate dendrite morphologies parallel with the ventricular wall. Open arrowheads denote GFP$^+$ neurons not containing onecut-3 signal (see also **Supplementary Fig. 7d**). (**f**) In-plane rendering of lightsheet microscopy reconstruction of the anterior–posterior distribution of dopamine-4 subclass (yellow label) along the wall of the third ventricle (see also **Supplementary Videos 1** and **2**). A13, zona incerta dopamine neurons, A14, PeVN dopamine neurons[27], A12, arcuate nucleus dopamine neurons[5]; 3V, third ventricle; PVN, paraventricular nucleus, Rch, retrochiasmatic area. (**g**) A molecularly equivalent dopamine neuron subclass with coexistence of phospho-Ser40-TH and onecut-3 exists in the human hypothalamus. Scale bars: 300 µm (**d**), 160 µm (**f**), 70 µm (**e**, **g** top), 7 µm (**g** bottom).

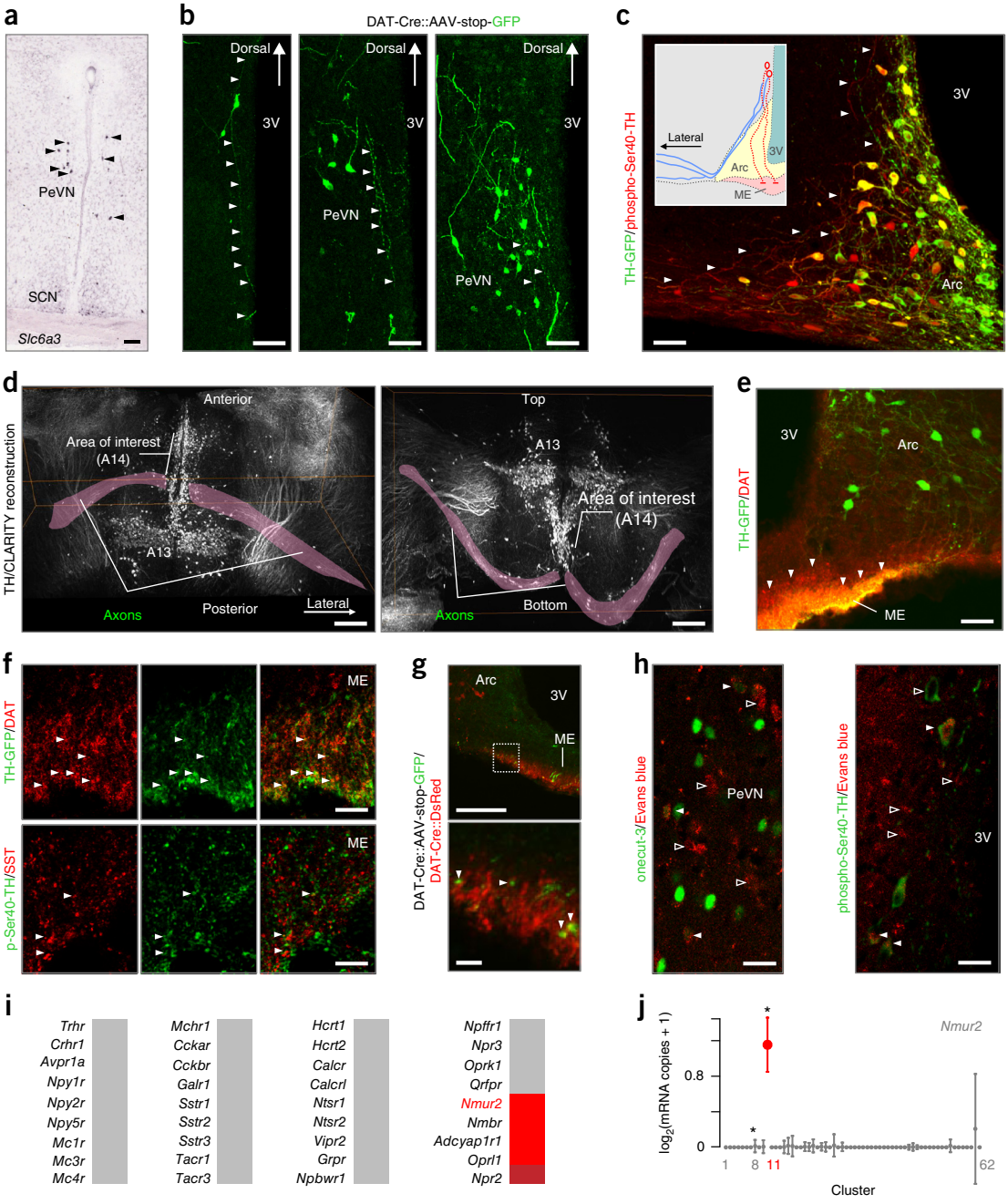

Figure 6 Efferent projections of periventricular onecut-3$^+$ dopamine neurons. (**a**) Dopamine transporter (*Slc6a3*) localization by *in situ* hybridization (http://www.brain-maps.org/) reveals a *Slc6a3*$^+$ cell cluster in the periventricular nucleus (arrowheads). (**b**) Microinjection of AAV-stop-GFP viruses into the periventricular region of *Dat1-Cre* mice reveals the morphology of periventricular *Dat1*$^+$ neurons, including their ramifying dendrites and axons primarily running ventrally and, in some cases, laterally. Arrowheads point to vertical axon-like projections. (**c**) By exploiting the association of exceptionally high phospho-Ser40-TH expression and low GFP fluorescence to distinguish periventricular neurons (see also **Supplementary Fig. 7c**), their phospho-Ser40-TH$^+$ axons (arrowheads) were confirmed to extend toward the median eminence (towards the midline, third ventricle; red in inset) as well as laterally (blue in inset). (**d**) Lightsheet microscopy optimized for CLARITY reconstruction of TH immunoreactivity with a focus on axons (magenta overlay) emanating from A14 and A12 cells. Lateral projections course toward amygdaloid nuclei. Horizontal (left) and coronal (right) views are shown, revealing an axonal detour around the ventromedial and lateral hypothalamic nuclei. (**e**) DAT-immunoreactive terminals at the median eminence (ME) of adult mice (arrowheads). (**f**) Colocalization of DAT, but not somatostatin (SST), and GFP fluorescence (arrowheads) at the ME in *Th-GFP* mice. (**g**) A *Dat1-Cre*::AAV-stop-GFP viral labeling confirmed that DAT$^+$ terminals (arrowheads) at the ME could originate, at least in part, in the periventricular nucleus; bottom, high-resolution image. (**h**) Systemic Evans blue administration led to its uptake by neurons residing in the periventricular nucleus and immunoreactive for onecut-3 (left) or phospho-Ser40-TH (right). Filled arrowheads pinpoint colocalization; open arrowheads denote neurosecretory cells whose identity was not pursued in this study. (**i**) Single-cell RNA-seq analysis of the receptor repertoire of onecut-3$^+$ dopamine neurons. Incremental mRNA expression was color coded as gray (no or sporadic expression; the mean of logarithmic value less than 2 s.e.m.), dark red (the mean of logarithmic value exceeding 2 s.e.m.) and red (the mean of logarithmic value with correction for the fraction of positive cells exceeding 2 s.e.m.). (**j**) Dopamine-4 subclass (cluster 11) predominantly expresses neuromedin U receptor 2 (*Nmur2*). *$q < 0.05$ (Wilcoxon rank-sum test corrected for multiple testing). Scale bars: 100 µm (**a**, **b**, **g** top), 70 µm (**c**,**e**), 180 µm (**d**), 40 µm (**f**, **h**), 10 µm (**g** bottom). 3V, third ventricle; Arc, arcuate nucleus; PeVN, periventricular nucleus; SCN, suprachiasmatic nucleus.

eminence as a potential release site for A14 neurons. Indeed, viral GFP transduction in *Dat1-Cre* mice confirmed the presence of median eminence–oriented projections and likely terminals (**Fig. 6g**). These data cumulatively suggest that A14 dopamine neurons might, at least in part, be classified as neuroendocrine cells releasing their dopamine content directly into the portal circulation (not excluding projections to the intermediate lobe of the pituitary)[6,31]. We tested this hypothesis by peripheral Evans blue dye loading, since circulating Evans blue does not cross the blood brain barrier and accumulates only in central neuronal somata that have access to the peripheral circulation. Twenty-four to 48 h after intraperitoneal dye loading, we found a subset of onecut-3$^+$ or phospho-Ser40-TH$^+$ neurons in the periventricular nucleus that accumulated Evans blue (**Fig. 6h**). Thus, we suggest that A14 dopamine neurons are bona fide neurosecretory cells (see also ref. 31), which are integrated into hypothalamic and/or extrahypothalamic neuronal networks. These data also recapitulate the known dichotomy of hypothalamic dopamine neurons either releasing their contents at the median eminence into the hypophyseal portal system[29] or using DAT to remove superfluous dopamine at central synapses.

Dopamine-4 neurons are entrained by neuromedin S

Next we explored whether dopamine-4 cells (cluster 11) receive specific afferentation that could contribute to their function. To this end, we mapped the receptor repertoire of dopamine-4 neurons by screening the expression of 36 neuropeptide receptors found by single-cell RNA-seq. Dopamine-4 cells abundantly expressed *Nmur2* (neuromedin U receptor 2), *Nmbr* (neuromedin B receptor), *Adcyap1r1* (adenylate cyclase activating polypeptide 1 receptor type I) and *Oprl1* (opiate receptor-like 1) (**Fig. 6i**). Whereas *Adcyap1r1* and *Oprl1* were promiscuously expressed in most neuronal clusters (data not shown), *Nmur2* and *Nmbr* were highly specific for dopamine-4 neurons (**Figs. 5a** and **6j**).

Neuromedin S is the endogenous agonist at neuromedin U receptor 2, with its production being concentrated in the SCN[32]. Indeed, our single-cell RNA-seq confirmed that neuromedin S (*Nms*) was present in all hypothalamic neurons that formed cluster 41 (**Fig. 7a**). The combination of RNA and positional information allowed us to predict an intrahypothalamic network to tune periventricular dopamine-4 output through the release of neuromedin S (**Fig. 7a**). Of note, 42% of *Nms*-expressing neurons in the SCN coexpressed *Vip* (**Fig. 7a**). Meanwhile, other *Vip*$^+$ neurons that were *Grp*$^+$ or *Grp*$^-$ and *Nms*$^-$ clustered separately (**Fig. 7a** and **Supplementary Fig. 8a**,**b**). Subsequent histochemistry validated these data by spatially confining neuromedin S production to the SCN (**Fig. 7b**)[32]. Moreover, the partial colocalization of neuromedin S with vasoactive intestinal peptide (VIP) (**Fig. 7b**) and of VIP with gastrin releasing peptide (GRP) within the SCN and in apposition to its periventricular targets (**Supplementary Fig. 8c**) lent further support to our RNA-seq-based prediction of neuronal network wiring. Finally, we used high-resolution laser-scanning microscopy to show that onecut-3$^+$ TH$^+$ double-positive neurons (focusing on those with particularly low *Th*-driven GFP levels, in accord with **Supplementary Fig. 7c**) receive neuromedin S$^+$ input (**Fig. 7b**). Thus an SCN–periventricular nucleus intrahypothalamic network may rely on neuromedin S as neuropeptide modulator. Nevertheless, our histochemical data do not exclude the possibility that dopamine-4 neurons in the periventricular nucleus might receive neuromedin S–containing inputs of extrahypothalamic origin.

Neuromedin S$^+$ neurons of the circadian pacemaker may modulate dopamine-4 cells

The presence of neuromedin S immunoreactivity in the periventricular nucleus prompted us to test whether this neuropeptide could affect

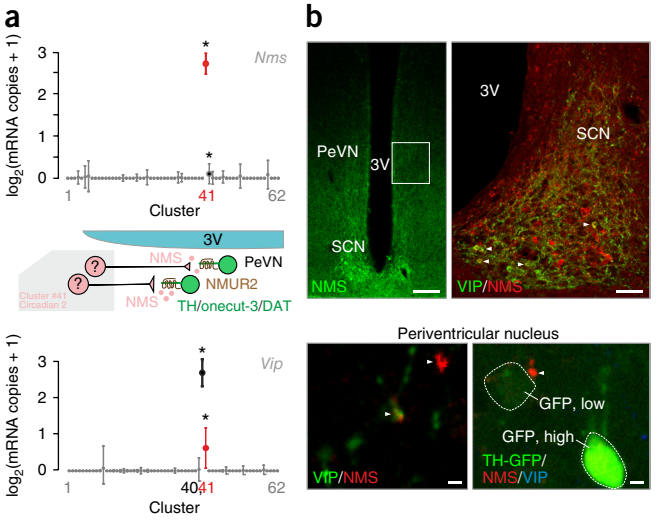

Figure 7 Suprachiasmatic origin for neuromedin S inputs to onecut-3$^+$ Nmur2$^+$ A14 dopamine neurons. (**a**) Top: single-cell RNA-seq revealed highest neuromedin S (*Nms*) expression by cluster 41 (circadian 2) in the mouse hypothalamus. $^*q < 0.05$ (Wilcoxon rank-sum test corrected for multiple testing). Middle: this ligand–receptor relationship allowed us to suggest a wiring diagram in which *Nms*-containing neurons of the suprachiasmatic nucleus can selectively innervate NMUR, TH, DAT and onecut-3-coexpressing periventricular dopamine neurons. Bottom: likewise, neurons in cluster 41 coexpressed vasoactive intestinal polypeptide (*Vip*). (**b**) Top: neuromedin S detection by histochemistry in the suprachiasmatic nucleus (SCN). Right panel shows neuromedin S and VIP coexistence in the SCN (filled arrowheads pointing to yellow composite color). Open rectangle denotes the general location of images shown below. Bottom: high-resolution analysis showed NMS$^+$ boutons (filled arrowheads, left) in the periventricular area, which preferentially terminated in close apposition to dopamine neurons (arrowhead, right) marked by low GFP expression in *Th-GFP* reporter mice. Scale bars: 100 µm (**b**, top left), 40 µm (**b**, top right), 6 µm (**b**, bottom). 3V, third ventricle; PeVN, periventricular nucleus.

dopamine-4 neurons through intercellular signaling. Therefore, we first mapped whether neuromedin S coexists with ubiquitous members of the SNARE synaptic vesicle release machinery. We indeed found that neuromedin S colocalized with vesicle-associated membrane protein 2 (VAMP2), marking presynapses, in close apposition to predominantly proximal dendrites of TH$^+$ and onecut-3$^+$ periventricular neurons (**Fig. 8a**). Subsequently, we deployed Ca^{2+} imaging with FURA2-AM to show that a subset (~7%) of periventricular dopamine neurons (expressing *Th*-driven GFP) exhibited resolvable Ca^{2+} responses upon acute application of neuromedin S (500 nM), using KCl as positive control (**Fig. 8b**).

Even though the exact physiological role of neuromedin S is still debated, earlier data implicates it in circadian regulation[32]. Indeed, our single-cell RNA-seq data showed that 42% of *Nms*$^+$ cluster 41 neurons coexpressed the gene period circadian clock-3 (*Per3*) (**Supplementary Fig. 8e**)[33]. Likewise, 25% of neuromedin S$^+$ neurons in cluster 41 coexpressed the primary pacemaker period circadian clock-2 (*Per2*)[34]. Notably, *Per2* was also expressed in cluster 42 (**Fig. 8c** and **Supplementary Fig. 8f**), where 23% of *Per2*$^+$ neurons expressed *Nms* (**Supplementary Fig. 8d**). These data predict that neuromedin S production might undergo circadian fluctuation. Therefore, we tested neuromedin S content in the SCN during day and night conditions and confirmed circadian-rhythm-driven oscillations in neuromedin S levels (**Fig. 8d**).

If neuromedin S production is under circadian regulation and, as suggested by our data, in a position to act on dopamine-4 neurons,

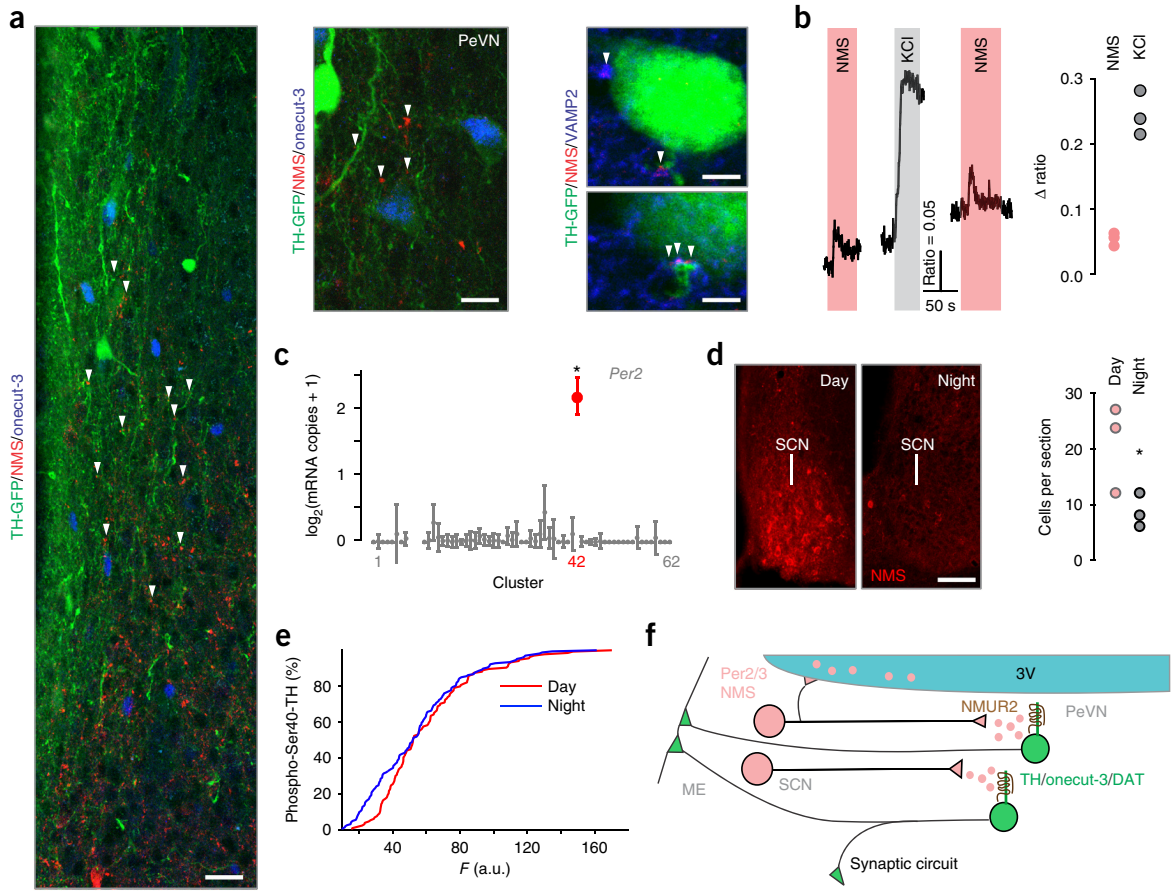

Figure 8 Periventricular onecut-3$^+$ dopamine neurons respond to neuromedin S produced during light periods. (**a**) Left and middle: immunohistochemical identification of synaptic contacts containing neuromedin S, which innervate onecut-3$^+$ A14 neurons. Right: VAMP2 was used as a ubiquitous presynaptic marker; perisomatic terminals are shown. (**b**) Bath application of 500 nM neuromedin S (NMS) leads to the generation of Ca^{2+} responses in a subset of periventricular TH$^+$ cells, which were scaleable to those produced by depolarization by 55 mM KCl. (**c**) The neuronal cluster containing neuromedin S (cluster 42) also expresses the circadian pacemaker gene *Per2*. Red symbol denotes significant expression (>2 s.e.m. from baseline); $*q < 0.05$. (**d**) Left panels: circadian fluctuations in neuromedin S content in the suprachiasmatic nucleus (SCN) as detected histochemically. Right, quantitative neuromedin S histochemistry using perisomatic fluorescence analysis on SCN neurons ($n = 3$ animals per group). $*P < 0.05$. (**e**) Circadian dependence of tyrosine hydroxylase phosphorylation at Ser40 as revealed by quantitative histochemistry ($n = 4$ animals per group). Cumulative distribution function is shown. $P = 0.0167$ (two-sample Kolmogorov-Smirnov test); *F*, fluorescence intensity. (**f**) Synaptic wiring of a circadian pacemaker network regulating dopamine release from A14 neurons in the periventricular nucleus of the hypothalamus. Both synaptic and volume transmission mechanisms for neuromedin S modulation of dopaminergic output at the median eminence (ME) might exist. Scale bars: 20 µm (**a**, left), 10 µm (**a**, middle), 5 µm (**a**, right top), 3 µm (**a**, right bottom), 50 µm (**d**).

then the latter might be expected to show phase shifts. Therefore, we monitored TH phosphorylation at Ser40, known to mark increased enzymatic activity and dopamine production[26]. This mark showed a distinct difference in the rising slope of the cumulative distribution function ($P = 0.0167$), suggesting different levels of active TH enzyme during day and night periods (**Fig. 8e**). Overall, these data highlight the fact that periventricular dopamine output is coupled to the circadian clock through the recruitment of a neuromedin S–containing excitatory projection between the SCN and periventricular nucleus[7].

Neuromedin S release sites

Besides their release at central synapses, some neuropeptides undergo regulated release into the cerebrospinal fluid (CSF) to mediate volume transmission[35,36]. We found neuromedin S$^+$ VAMP2$^+$ inputs to TH$^+$ onecut-3$^+$ neurons concentrated mostly in the rostral subdivision of the periventricular nucleus, positioned above the SCN. Since we could not find a similar gradient of *Nmur2* expression (Allen Brain Atlas, experiment 81600118), neuromedin S release into the CSF would reconcile this difference and provide an alternative means of long-distance signaling. Unexpectedly, we identified neuromedin S$^+$ nerve endings along the wall of the third ventricle at the level of the anterior part of the median eminence (**Supplementary Fig. 8g**). These data, together with the recent identification of neuromedin S in human CSF[35], suggest that ventricle-oriented release sites might exist to allow volume transmission as an alternative to synaptic or nonsynaptic communication within the periventricular nucleus (**Fig. 8f**).

DISCUSSION

Our knowledge of neuronal subtypes in the neocortex, hippocampus and cerebellum, together with the origins and layer distribution of synaptic inputs[9,37,38], has led to robust structure–function studies that uncovered key cellular substrates of higher cognitive and motor functions. In contrast, the study of brain regions that contain many functionally distinct but positionally interspersed neuronal subtypes in small volumes, such as the hypothalamus, remains a challenge.

Here we combined single-cell RNA-seq of hypothalamic neurons, spatially resolved circuit mapping and functional assays to (i) pioneer the molecular study of neuronal organization; (ii) detect dual (or even triple) neurotransmitter phenotypes (**Fig. 3**), assuming their activity-dependent switching; (iii) examine receptor repertoires for circuit prediction; and (iv) resolve existing ambiguities in neuronal nomenclature by unifying neurotransmitter-neuropeptide relationships. Notably, we also detected many mRNAs previously localized to neurites[39]. Therefore, sequencing somatic contents will likely produce a representative catalog of total mRNAs expressed by a single neuron.

The computational algorithms used here include tSNE and BackSpin. tSNE is a pure dimensional reduction algorithm and was used only for the visualization of multidimensional data. BackSpin, in turn, is not based on dimensional reduction but on a series of binary splits, which allow focusing on the most relevant set of genes while clustering a subset of cells. Taking into account the high neuronal diversity of the hypothalamus, as confirmed by both analysis routines, we consider these results (**Supplementary Figs. 3** and **4**) as a mutual cross-validation of both approaches.

Our molecular profiling focused on the central column of the hypothalamus, leaving its most lateral and caudal segments uncharted. Therefore, we presume that further neuronal subtypes, divergent either at the molecular or functional levels, might be revealed by sequencing tools that can process larger volumes of data, such as Drop-seq[22]. Thus, one might predict that the number of neuronal subtypes in the mammalian hypothalamus could reach beyond 100. During our effort to reconstruct neuronal networks through a combination of RNA-seq on dissociated cells and subsequent bioinformatics as predictive tools ('forward transcriptomics'), we discovered a distinct subtype of dopamine neurons, dopamine-4 cells, situated in the A14 locus, whose molecular phenotype challenges the concept of a dopamine continuum in the hypothalamus. We propose that adjacent blocks of phenotypically distinct dopamine cells assemble an anatomically continuous stream of cells that, when using known markers, such as TH, seems homogeneous. This principle might be applicable to other subtypes of hypothalamic neurons as well, and therefore the resource we offer can inform many structure–function studies addressing key outputs of hypothalamic neuronal circuits.

Any new method requires extensive validation. As an example, we studied the expression of some receptors regulating body metabolism through sensing ligand levels in the general circulation. In particular, our data revealed that pancreatic polypeptide receptor (*Npy6r*) mRNA was confined to circadian neurons coexpressing *Vip* and *Nms* (cluster 41), leaving *Vip*-only neurons of the neighboring circadian cluster (40) unchecked. This result lends support to previous data[40] and advances knowledge in receptor-dependent function determination for pancreatic polypeptide. Similarly, our analysis of leptin receptor (*Lepr*) expression, whose activity upon binding white fat–derived leptin[41] is associated with satiety, showed that *Lepr* was expressed at low levels (1 mRNA copy per cell) and detected in only ~3% of hypothalamic neurons. The low number of *Lepr*$^+$ neurons we found is in contrast to the high numbers of cells identified in studies using *Lepr-Cre*-driven GFP expression in mice[42]. This discrepancy can be explained by the temporal snapshot nature of our RNA-seq strategy, as compared to GFP-expressing animals that reflect the accumulated expression over the animal's lifetime, as corroborated by our own *Crh-IRES-Cre::stop-GFP* (**Supplementary Fig. 5a**) and *Crh-EGFP* experiments[18], showing that episodic expression of any gene during the lifetime of a neuron might be a common feature. At the level of neuronal identity, 30% of the cell population coexpressing *Npy* and *Agrp* (4 of 13 cells) contained *Lepr* mRNAs. Moreover, we characterized *Lepr* mRNA expression in some glutamatergic neurons, corroborating published reports[42]. An additional strength of our data set is that it relies on both male and female animals kept under *ad libitum* feeding conditions, suggesting that we resolved ground-state *Lepr* mRNA expression, relevant for behavioral output in both sexes (see also **Supplementary Fig. 2a**). Finally, our results on acute formalin-injection-induced stress show that the formation of new neuronal clusters (that is, subtypes) does not occur under these circumstances, meaning that no new neuronal subtype is generated over hour-long timescales.

By consensus definition, each neuron is expected to contain at least one fast neurotransmitter, which can be co-released with another neurotransmitter (for example, dopamine), and one or more peptide, gaseous or lipid neuromodulators[20,43–45]. Using the abundance of mRNAs for neurotransmitter-producing enzymes and vesicular and reuptake transporters as a weighting factor (**Fig. 2b**), non-*Oxt*/non-*Avp* neurons were subdivided into primarily dopaminergic, GABAergic and glutamatergic subtypes. Yet, and in contrast to RNA-seq data on cortical neurons[9], we found unexpected combinations of neurotransmitters in an estimated 18% of hypothalamic neurons. Therefore, nominal classification as dopaminergic, GABAergic or glutamatergic (single-neurotransmitter criteria) must be used with care because metabolic pathways for alternative neurotransmitters could coexist (**Fig. 3**). These might be bioenergetically more favorable than rewiring strategies[16,17]. When comparing single-cell RNA-seq data from cortical or hippocampal versus hypothalamic neurons, the following differences apply: (i) in the cerebral cortex, higher mRNA transcript levels are seen in interneurons, which also contain both *Gad1* and *Gad2* transcripts, than in their hypothalamic equivalents and (ii) cortical neurons rarely, if ever, have mixed excitatory and inhibitory phenotypes[9]. Thus, the molecular makeup of hypothalamic neurons differs from that of their cortical counterparts. Yet, given their statistical prevalence, mixed neurotransmitter phenotypes are not an exception but rather may be a general principle. This arrangement could contribute to the flexibility of hypothalamic neuronal networks in adapting to ever-changing environmental stimuli.

Addressing the range of systemic consequences of hormone release at the median eminence has been at the forefront of neuroendocrinology research for decades[2]. For dopamine, parvocellular dorsomedial neurosecretory cells (*Th*$^+$) in the Arc (A12) give rise to large nerve endings in the median eminence, amassing one-third of all boutons in the lateral external layer[46], and release dopamine for the tonic inhibition of pituitary prolactin release[29]. For dopamine neurons in the periventricular nucleus (A14), a significant intrahypothalamic drive from the SCN has been established[7,8,47]. This synaptic circuit is noteworthy because it integrates the circadian pacemaker (characterized by *Per* genes)[33,34] and hormonal output, particularly diurnally fluctuating dopamine levels in the general circulation[7]. By histochemistry, we showed that onecut-3$^+$ A14 dopamine neurons can terminate at the median eminence. Notably, the results of our Evans blue loading experiments are also in agreement with a previously documented parallel projection to the intermediate lobe of the pituitary[31]. Our data outline a potential cellular substrate that may participate in dopamine release into the hypophyseal portal system and/or the intermediate lobe for the chronospecific inhibition of pituitary prolactin secretion[29] (**Fig. 6g**,**h**). Such a role is in agreement with indications that periventricular dopamine cells are involved in the feedback control of prolactin release[48]. These newly distinguished neurons are exclusively situated at the medio-posterior subdivision of the periventricular area and receive *Nms*$^+$ synaptic afferents from SCN neurons regulating the circadian clock[32,49], in addition to the expression of clock

genes in the periventricular and Arc dopamine cells themselves[50]. Thus, these onecut-3$^+$ TH$^+$ neurons can also serve as neurosecretory 'hubs' to tune the release of many other hypothalamic neuropeptides through synaptic afferents. Cumulatively, we recognize onecut-3$^+$ A14 dopamine neurons as distinctly different, at the level of molecular makeup and connectivity, from the dorsomedial A12 dopamine group, thus showcasing that single-cell RNA-seq in combination with neuroanatomy can produce a molecular protomap of hypothalamic neuronal organization and aid the future discovery of functionally segregated neuronal subclasses.

METHODS

Methods, including statements of data availability and any associated accession codes and references, are available in the online version of the paper.

Note: Any Supplementary Information and Source Data files are available in the online version of the paper.

ACKNOWLEDGMENTS

The authors thank N.-G. Larsson and L. Olson for providing *Dat1-Cre* mice for the generation of reporter mice, H. Wong and M. Watanabe for antibodies and K. Meletis for his supervision of viral injections in *Dat1*-Cre mice. This work was supported by the Swedish Research Council (T. Harkany, T. Hökfelt, S.L., C. Broberger), Hjärnfonden (T. Harkany), the Petrus and Augusta Hedlunds Foundation (T. Harkany), the Novo Nordisk Foundation (T. Harkany, T. Hökfelt, C. Broberger), the National Brain Research Program of Hungary (MTA-SE NAP B, KTIA_NAP_13-2014-0013; A.A.), the European Commission (PAINCAGE grant, T. Harkany, T. Hökfelt), the European Research Council (BRAINCELL; S.L., ENDOSWITCH; C. Broberger and SECRET-CELLS; T. Harkany), intramural funds of the Medical University of Vienna (T. Harkany) and an NIH grant AG051459 (T.L.H.). R.A.R. is an EMBO long-term research fellow (ALTF 596-2014) cofunded by the European Commission FP7 (Marie Curie Actions, EMBOCOFUND2012, GA-2012-600394). A.Z. received support from the Human Frontier Science Program. F.C. is a Research Associate of the Fonds de la Recherche Scientifique-FNRS, Belgium. The single-cell sequencing infrastructure at CeMM was supported by a New Frontiers Research Infrastructure grant from the Austrian Academy of Sciences.

AUTHOR CONTRIBUTIONS

T. Harkany and R.A.R. conceived the general framework of this study. T. Harkany, T.L.H., S.L., R.A.R., A.Z., T. Hökfelt, C. Broberger, K.D. designed experiments, T. Harkany, T.L.H., S.L., T. Hökfelt, C. Broberger, K.D., A.A., J.M. and C. Bock senior authors, sponsored research. R.A.R., A.Z., A.H., J.B., F.G., A.A., E.K., R.T., B.H., A.K.C., D.C., M.-D.Z., A.R. and M.F. performed research and analyzed data. H.M., C.S., D.C., Z.M., G.S., F.C., Y.Y., M.U., J.S.B. and P.W. provided unique reagents. R.A.R., A.Z., T.L.H. and T. Harkany wrote the paper. All authors reviewed the manuscript and approved its submission.

COMPETING FINANCIAL INTERESTS

The authors declare competing financial interests: details are available in the online version of the paper.

1. Du Vigneaud, V. Hormones of the posterior pituitary gland: oxytocin and vasopressin. *Harvey Lect.* **50**, 1–26 (1954-1955).
2. Clarke, I.J. Hypothalamus as an endocrine organ. *Compr. Physiol.* **5**, 217–253 (2015).
3. Lantos, T.A., Görcs, T.J. & Palkovits, M. Immunohistochemical mapping of neuropeptides in the premamillary region of the hypothalamus in rats. *Brain Res. Brain Res. Rev.* **20**, 209–249 (1995).
4. Swanson, L.W. & Kuypers, H.G. The paraventricular nucleus of the hypothalamus: cytoarchitectonic subdivisions and organization of projections to the pituitary, dorsal vagal complex, and spinal cord as demonstrated by retrograde fluorescence double-labeling methods. *J. Comp. Neurol.* **194**, 555–570 (1980).
5. Dahlström, A. & Fuxe, K. Evidence for existence of monoamine-containing neurons in central nervous system. I. Demonstration of monoamines in cell bodies of brain stem neurons. *Acta Physiol. Scand. Suppl.* **62** (Suppl. 232): 1–55 (1964).
6. Björklund, A., Moore, R.Y., Nobin, A. & Stenevi, U. The organization of tubero-hypophyseal and reticulo-infundibular catecholamine neuron systems in the rat brain. *Brain Res.* **51**, 171–191 (1973).
7. Horvath, T.L. Suprachiasmatic efferents avoid phenestrated capillaries but innervate neuroendocrine cells, including those producing dopamine. *Endocrinology* **138**, 1312–1320 (1997).
8. Abizaid, A., Horvath, B., Keefe, D.L., Leranth, C. & Horvath, T.L. Direct visual and circadian pathways target neuroendocrine cells in primates. *Eur. J. Neurosci.* **20**, 2767–2776 (2004).
9. Zeisel, A. *et al.* Brain structure. Cell types in the mouse cortex and hippocampus revealed by single-cell RNA-seq. *Science* **347**, 1138–1142 (2015).
10. Scott, N., Prigge, M., Yizhar, O. & Kimchi, T. A sexually dimorphic hypothalamic circuit controls maternal care and oxytocin secretion. *Nature* **525**, 519–522 (2015).
11. Yang, C.F. *et al.* Sexually dimorphic neurons in the ventromedial hypothalamus govern mating in both sexes and aggression in males. *Cell* **153**, 896–909 (2013).
12. Xu, X. *et al.* Modular genetic control of sexually dimorphic behaviors. *Cell* **148**, 596–607 (2012).
13. Yang, X. *et al.* Tissue-specific expression and regulation of sexually dimorphic genes in mice. *Genome Res.* **16**, 995–1004 (2006).
14. Dulcis, D., Jamshidi, P., Leutgeb, S. & Spitzer, N.C. Neurotransmitter switching in the adult brain regulates behavior. *Science* **340**, 449–453 (2013).
15. Meister, B., Cortés, R., Villar, M.J., Schalling, M. & Hökfelt, T. Peptides and transmitter enzymes in hypothalamic magnocellular neurons after administration of hyperosmotic stimuli: comparison between messenger RNA and peptide/protein levels. *Cell Tissue Res.* **260**, 279–297 (1990).
16. Pinto, S. *et al.* Rapid rewiring of arcuate nucleus feeding circuits by leptin. *Science* **304**, 110–115 (2004).
17. Cristino, L. *et al.* Obesity-driven synaptic remodeling affects endocannabinoid control of orexinergic neurons. *Proc. Natl. Acad. Sci. USA* **110**, E2229–E2238 (2013).
18. Romanov, R.A. *et al.* A secretagogin locus of the mammalian hypothalamus controls stress hormone release. *EMBO J.* **34**, 36–54 (2015).
19. Henry, F.E., Sugino, K., Tozer, A., Branco, T. & Sternson, S.M. Cell type-specific transcriptomics of hypothalamic energy-sensing neuron responses to weight-loss. *Elife* **4**, 09800 (2015).
20. Krashes, M.J. *et al.* An excitatory paraventricular nucleus to AgRP neuron circuit that drives hunger. *Nature* **507**, 238–242 (2014).
21. Everitt, B.J., Hökfelt, T., Wu, J.Y. & Goldstein, M. Coexistence of tyrosine hydroxylase-like and gamma-aminobutyric acid-like immunoreactivities in neurons of the arcuate nucleus. *Neuroendocrinology* **39**, 189–191 (1984).
22. Macosko, E.Z. *et al.* Highly parallel genome-wide expression profiling of individual cells using nanoliter droplets. *Cell* **161**, 1202–1214 (2015).
23. Lee, S.Y., Földy, C., Szabadics, J. & Soltesz, I. Cell-type-specific CCK2 receptor signaling underlies the cholecystokinin-mediated selective excitation of hippocampal parvalbumin-positive fast-spiking basket cells. *J. Neurosci.* **31**, 10993–11002 (2011).
24. Moriya, R. *et al.* RFamide peptide QRFP43 causes obesity with hyperphagia and reduced thermogenesis in mice. *Endocrinology* **147**, 2916–2922 (2006).
25. Zagorácz, O. *et al.* Effects of direct QRFP-26 administration into the medial hypothalamic area on food intake in rats. *Brain Res. Bull.* **118**, 58–64 (2015).
26. Tekin, I., Roskoski, R. Jr., Carkaci-Salli, N. & Vrana, K.E. Complex molecular regulation of tyrosine hydroxylase. *J. Neural Transm.* **121**, 1451–1481 (2014).
27. Hökfelt, T., Martensson, R., Bjorklund, A., Kleinau, S. & Goldstein, M. Distribution maps of tyrosine-hydroxylase-immunoreactive neurons in the rat brain. in *Handbook of Chemical Neuroanatomy* (eds. Bjorklund, A. & Hökfelt, T.) 277–379 (Elsevier, 1984).
28. Meister, B. & Elde, R. Dopamine transporter mRNA in neurons of the rat hypothalamus. *Neuroendocrinology* **58**, 388–395 (1993).
29. Ben-Jonathan, N. & Hnasko, R. Dopamine as a prolactin (PRL) inhibitor. *Endocr. Rev.* **22**, 724–763 (2001).
30. Stagkourakis, S., Kim, H., Lyons, D.J. & Broberger, C. Dopamine autoreceptor regulation of a hypothalamic dopaminergic network. *Cell Rep.* **15**, 735–747 (2016]).
31. Goudreau, J.L., Lindley, S.E., Lookingland, K.J. & Moore, K.E. Evidence that hypothalamic periventricular dopamine neurons innervate the intermediate lobe of the rat pituitary. *Neuroendocrinology* **56**, 100–105 (1992).
32. Mori, K. *et al.* Identification of neuromedin S and its possible role in the mammalian circadian oscillator system. *EMBO J.* **24**, 325–335 (2005).
33. Zhang, L. *et al.* A PERIOD3 variant causes a circadian phenotype and is associated with a seasonal mood trait. *Proc. Natl. Acad. Sci. USA* **113**, E1536–E1544 (2016).
34. Vitaterna, M.H. *et al.* Differential regulation of mammalian period genes and circadian rhythmicity by cryptochromes 1 and 2. *Proc. Natl. Acad. Sci. USA* **96**, 12114–12119 (1999).
35. Hölttä, M. *et al.* An integrated workflow for multiplex CSF proteomics and peptidomics-identification of candidate cerebrospinal fluid biomarkers of Alzheimer's disease. *J. Proteome Res.* **14**, 654–663 (2015).
36. Irani, D.N. Properties and composition of normal cerebrospinal fluid. in *Cerebrospinal Fluid in Clinical Practice* Ch. 10, 69–89 (W.B. Saunders, Philadelphia, 2009).
37. Bro, S. & Haycock, J.W. Visual cortex (translation of Ramón y Cajal, S.) translated from *L'Encorce Cérébrale Suivant les Régions L'Ecorce Visuelle*, Ch. 25 in *Histologie du Système Nerveux de l'Homme et des Vertébrés*, 1911. *Behav. Biol.* **21**, 508–528 (1977).

38. Ascoli, G.A. *et al.* Petilla terminology: nomenclature of features of GABAergic interneurons of the cerebral cortex. *Nat. Rev. Neurosci.* **9**, 557–568 (2008).
39. Zivraj, K.H. *et al.* Subcellular profiling reveals distinct and developmentally regulated repertoire of growth cone mRNAs. *J. Neurosci.* **30**, 15464–15478 (2010).
40. Yulyaningsih, E. *et al.* Pancreatic polypeptide controls energy homeostasis via Npy6r signaling in the suprachiasmatic nucleus in mice. *Cell Metab.* **19**, 58–72 (2014).
41. Friedman, J.M. & Halaas, J.L. Leptin and the regulation of body weight in mammals. *Nature* **395**, 763–770 (1998).
42. Scott, M.M. *et al.* Leptin targets in the mouse brain. *J. Comp. Neurol.* **514**, 518–532 (2009).
43. Boulland, J.L. *et al.* Vesicular glutamate and GABA transporters sort to distinct sets of vesicles in a population of presynaptic terminals. *Cereb. Cortex* **19**, 241–248 (2009).
44. Dawson, T.M. & Snyder, S.H. Gases as biological messengers: nitric oxide and carbon monoxide in the brain. *J. Neurosci.* **14**, 5147–5159 (1994).
45. Jonas, P., Bischofberger, J. & Sandkühler, J. Corelease of two fast neurotransmitters at a central synapse. *Science* **281**, 419–424 (1998).
46. Ajika, K. & Hökfelt, T. Ultrastructural identification of catecholamine neurones in the hypothalamic periventricular-arcuate nucleus-median eminence complex with special reference to quantitative aspects. *Brain Res.* **57**, 97–117 (1973).
47. Horvath, T.L. An alternate pathway for visual signal integration into the hypothalamo-pituitary axis: retinorecipient intergeniculate neurons project to various regions of the hypothalamus and innervate neuroendocrine cells including those producing dopamine. *J. Neurosci.* **18**, 1546–1558 (1998).
48. DeMaria, J.E., Lerant, A.A. & Freeman, M.E. Prolactin activates all three populations of hypothalamic neuroendocrine dopaminergic neurons in ovariectomized rats. *Brain Res.* **837**, 236–241 (1999).
49. Lee, I.T. *et al.* Neuromedin s-producing neurons act as essential pacemakers in the suprachiasmatic nucleus to couple clock neurons and dictate circadian rhythms. *Neuron* **85**, 1086–1102 (2015).
50. Sellix, M.T. *et al.* Anatomical and functional characterization of clock gene expression in neuroendocrine dopaminergic neurons. *Am. J. Physiol. Regul. Integr. Comp. Physiol.* **290**, R1309–R1323 (2006).

ONLINE METHODS

Animals, tissue preparation and histochemistry. Single-cell RNA-seq and histochemistry were conducted in mice on a C57BL/6N background before sexual maturation during postnatal days (P) 14–28. Transgenic animals were also on C57BL/6N backgrounds either from their generation or through backcrossing for multiple generations. The reporter lines *GAD67*$^{+/gfp}$, *GAD67*$^{+/gfp}$*::CCK*$^{BAC/DsRedT3}$ (refs. 51, 52), *B6.B6D2-Tg(Th-EGFP)21-31Koba* (developed by K. Kobayashi and available from Riken Bioresource Center), *Crh-IRES-Cre::B6.Cg-Gt(ROSA)26Sor*$^{tm6(CAG-ZsGreen1)Hze}$/J (*Ai6*; both GFP reporters were from the Jackson Laboratories, cat. nos. 012704 and 007906) and dopamine transporter *Dat1-Cre::B6.Cg-Gt(ROSA)26Sor*$^{tm14(CAG-tdTomato)Hze}$/J mice were extensively validated and used for neuronal identity mapping by histochemistry (n = 3–5 per group). Animals were housed conventionally (12-h/12-h light cycle, 55% humidity). Experimental protocols were in accordance with the European Communities Council Directive (86/609/EEC), approved by regional ethical committees and regulated by applicable local laws (Stockholms Norra Djurförsöksetiska Nämnd; N512/12 (Sweden) and Tierversuchsgesetz 2012, BGBI, Nr. 114/2012 (Austria)). Particular effort was directed toward minimizing the number of animals used and their suffering during experiments.

For histochemical evaluation, animals were transcardially perfused with a fixative composed of 4% paraformaldehyde (PFA) in 0.1 M phosphate buffer (PB; pH 7.4) that was preceded by a short pre-rinse with physiological saline (anesthesia: 5% isoflurane at 1 l/min). In experiments investigating circadian clock-related changes in neuromedin S production, transcardial perfusions were carried out during the periods of 10.00–11.00 (day, light) and 22.00–23.00 (night, dark). After overnight postfixation in the same fixative and cryoprotection in 30% sucrose for at least 48 h, 30–50-µm-thick serial free-floating or 16-µm-thick serial glass-mounted sections were cut on a cryostat microtome and processed for multiple immunofluorescence histochemistry according to published protocols[18]. (E)GFP and DsRed immunofluorescence were not amplified in any of the transgenic models. Free-floating sections were rinsed in PB (pH 7.4) and pretreated with 0.3% Triton X-100 (in PB) for 1 h at 22–24 °C to enhance antibody penetration. Nonspecific immunoreactivity was suppressed by incubating specimens in a cocktail of 5% normal donkey serum (NDS; Jackson), 1% bovine serum albumin (BSA; Sigma) and 0.3% Triton X-100 (Sigma) in PB for 1 h at 22–24 °C. Sections were then exposed to select combinations of primary antibodies diluted in PB containing 0.1% NDS and 0.3% Triton X-100 for 48 h at 4 °C. Primary antibodies were as follows: rabbit anti-oxytocin (1:5,000; Millipore, cat. no. Mab 5296), guinea pig anti-CRH (1:1,000; Peninsula, T-5007.0050), goat anti-neurophysin II (AVP; 1:50; Santa Cruz, cat. no. sc-27093), rabbit anti-tyrosine hydroxylase (TH) (1:1,000; Millipore, cat. no. AB152), mouse anti-TH (1:500; Millipore, cat. no. MAB5280), rabbit anti-phospho-Ser40-TH (1:1,000; Millipore, cat. no. AB5935), guinea pig anti-onecut-3 (1:5,000)[53], rat anti-somatostatin (1:250; Millipore, MAB354), rabbit anti-neuromedin S (1:1,000; Bachem, cat. no. T-4814.0400), mouse anti-vasoactive intestinal polypeptide[54] (1:400; kindly provided by Helen Wong, David Geffen School of Medicine, UCLA), rabbit anti-GRP (1:200, ImmunoStar, cat. no. 20073), mouse anti-synaptobrevin 2 (VAMP2) (1:200; Synaptic Systems, cat. no. 104211), rabbit anti-dopamine transporter (DAT) (1:250; Synaptic Systems, cat. no. 284003) and guinea pig anti-DAT (1:250; Synaptic Systems, cat. no. 284005). After extensive rinsing in PB, immunoreactivities were revealed using carbocyanine Cy2-, Cy3- or Cy5-tagged secondary antibodies raised in donkey (1:200; Jackson, cat. no. for rabbit: 711-225-152, 711-165-152, 711-175-152, 706-225-148; guinea pig: 706-165-148, 706-175-148; and mouse: 715-225-150, 715-165-150, 715-175-150; 2 h incubation at 22–24 °C). Sections were mounted on fluorescence-free glass slides and coverslipped with Entellan (in toluene; Merck).

For immunohistochemistry on glass-mounted cryosections, polyclonal rabbit antibodies against ARFGEF1 (1 µg/ml, HPA023822), USP48 (1 µg/ml, HPA030046), KIF5A (1 µg/ml, HPA004469; all available from Atlas Antibodies), guinea pig anti-AVP (1:1,200; Peninsula), rabbit anti-vesicular glutamate transporter 2 (VGLUT2, 1:400; gift from M. Watanabe[55], Hokkaido University School of Medicine) and mouse anti-GAD67 (1:400; Millipore MAB5406) were diluted in PB to which 0.3% Triton X-100 had been added for 16–24 h at 4 °C. Immunoreactivity was visualized using the tyramide signal amplification method (1:100, PerkinElmer)[56]. When applying Atlas antibodies, sections were counterstained with DAPI as nuclear marker and whole slides were captured using a 10× (Plan-Apocromat 10×/0.45 NA) primary objective on a Vslide slide-scanning microscope (Metasystems) equipped with appropriate filter sets. Individual field-of-view images were stitched to produce images of entire brain sections with high resolution. Extended image data on Atlas antibodies are available in the most recent version (HPA14) of the human protein atlas (http://www.proteinatlas.org/).

Systemic Evans blue administration. Neuroendocrine cells were identified by their uptake of systemically administered Evans blue[57]. Briefly, mice (n = 7) were bolus-injected i.p. with 0.25 ml of Evans blue (3%) dissolved in physiological saline and allowed to survive for an additional 24, 48 or 72 h. Brain slices containing the periventricular region were prepared on a vibratome (VT1200S, Leica), immersion-fixed in 4% PFA in 0.1 M PB, and imaged on a Zeiss LSM780 confocal microscope. Upon successful Evans blue uptake, brain slices were processed for the colocalization of TH, onecut-3 or phospho-Ser40-TH (as above).

Virus microinjection *in vivo*. Male *Dat1-Cre::B6.Cg-Gt(ROSA)26Sor*$^{tm14(CAG-tdTomato)Hze}$/J mice (2 months of age, n = 3) were used for the injection of AAV1/2-flex-GFP virus constructs as described[58,59]. Briefly, mice anesthetized by isoflurane (5%, 1 l/min) and placed in a stereotaxic frame (Harvard) were injected with 250–450 nl of virus (6×10^8 particles/ml) bilaterally using a micropipette coupled to a Quintessential stereotaxic injector (Stoelting). Injections targeted the periventricular nucleus at the following coordinates: anterior–posterior, −1.0 mm; lateral, ±0.2 mm; dorsoventral, −5.2 mm from dura mater. The micropipette was held in place for 5 min before slowly retracting it from the hypothalamus to limit virus spread. Buprenorphine (0.03 mg/kg) was applied for postsurgical analgesia. Procedures were approved by the regional authority (Stockholms Norra Djurförsöksetiska Nämnd; N166/15). After 14 d of survival, mice were reanesthetized with pentobarbital (50 mg/kg, i.p.) and perfused with 4% PFA containing 0.1% picric acid in 0.1 M PB (pH7.4). Whole brains were postfixed for 120 min in the same fixative at 4 °C, followed by rinses in 10% sucrose (in 0.1 M PB, pH 7.4) containing 0.01% sodium azide (Merck) and 0.02% bacitracin (Sigma) over 2–3 d at 4 °C. Brains were then embedded in 4% agarose in 0.05 M phosphate-buffered saline and coronal sections (60 µm) were cut on a vibratome (VT1000, Leica). For immunohistochemistry, free-floating sections were washed in PBS, incubated in 1% H_2O_2 (in PBS) for 10 min, and blocked in PBS containing 0.3% Triton-X and 5% NDS (Jackson) for 1 h at 22–24 °C. Specimens were then exposed to a chicken anti-GFP antibody (1:8,000; Abcam, cat. no. ab13970) at 4 °C overnight. Immunoreactivity was visualized using the TSA Plus kit (PerkinElmer) using a horseradish peroxidase–conjugated donkey anti-chicken antibody (1:200, 75 min, Jackson, 703-035-155). Finally, sections were incubated in biotinyl tyramide-fluorescein (1:100 in amplification diluent) for 10 min, mounted on SuperFrost Plus glass slides, air dried and coverslipped with 50% glycerol in PBS.

Laser-scanning and lightsheet microscopy by Lightsheet Z.1 in optically cleared hypothalami. Laser-scanning microscopy to obtain *x,y* (single plane) images was performed on a Zeiss 780LSM laser-scanning microscope at 40× or 63× primary magnification and with maximal signal separation or spectral unmixing. Quantitative determination of the colocalization of VGLUT2 and GAD67 immunoreactivities at the median eminence was undertaken at 40× primary magnification and by using the ZEN2013 software package (Zeiss) to define signal coexistence in red and green channels.

For lightsheet microscopy, hypothalami from *GAD67*$^{gfp/+}$ P23 mice were microdissected and cleared using a modified CUBIC protocol[60]. In brief, blocks of 4% PFA-fixed tissues were incubated, under continuous agitation in CUBIC 1 solution (25% urea, 25% *N,N,N′,N′*-tetrakis-(2-hydroxypropyl)ethylenediamine and 15% Triton X-100) at 37 °C for 4 d. Immunostainings were carried out after CUBIC 1 clearing. First, samples were washed three times for 30 min each in 0.1 M PB (pH 7.4) at 22–24 °C, during which tissues regained their opaque appearance. This was followed by a 6 h incubation in PB-based blocking solution containing 2.5% BSA, 5% NDS, 0.5% Triton X-100 and 10% DMSO. Sections were then incubated with rabbit anti-phospho-Ser40-TH (1:500; Millipore, cat. no. AB5935) and guinea pig anti-onecut-3 (1:1,000, ref. 53) primary antibodies diluted in PB containing 2% NDS, 0.1% BSA, 0.3% Triton X-100, 5% DMSO and 0.1% NaN_3 for 96 h at 37 °C with gentle shaking. Following three washes of 30 min each in PB, immunoreactivities were revealed by incubation in Cy2- and Cy3-tagged secondary antibodies (1:200; Jackson Laboratories, rabbit: 711-165-152;

doi:10.1038/nn.4462

guinea pig: 706-225-148) diluted in PB containing 3% NDS and 0.1% NaN_3 for 48 h at 22–24 °C. Samples subsequently underwent four washes of 60 min each in PB before immersion in CUBIC 2 solution (50% sucrose, 25% urea, 10% 2,2′,2′-nitrilotriethanol and 0.1% Triton X-100). Tissues were left to shake at 22–24 °C for 3 d before image acquisition. All samples were imaged in CUBIC 2 solution with a measured refractory index of 1.45. A sequence of fluorescence images was acquired on a Lightsheet Z.1 (Zeiss) microscope using a 5× detection objective, 5× illumination optics and laser excitation at 488 nm and 561 nm. Each plane was illuminated from a single side, and whole hypothalamic images were obtained through 3 × 4 tile scanning. All images were captured at 0.7× zoom, with *z*-stack intervals set at 3.0 µm with an exposure time of 250 ms and 600 ms for 561 nm (Cy3; phospho-Ser40-TH) and 488 nm (Cy2; one-cut-3) laser lines, respectively. 3D-rendered images were visualized with Arivis Vision4D for Zeiss (v. 2.12). Brightness and contrast of the 3D-rendered images were manually adjusted to aid visual clarity. Composite figures were assembled in CorelDraw X7 (Corel Corp.).

Whole-brain mapping by CLARITY. Reconstruction of TH-positive neurons and their projections in the intact adult mouse brain were performed using passive CLARITY methods as described[62]. Briefly, wild-type C57Bl6/N adult mouse brains were cleared using the passive CLARITY protocol (1%) hydrogel monomer solution followed by whole brain TH immunostaining using a polyclonal rabbit anti-TH antibody (1:50; Abcam, cat. no. ab113). High-resolution whole brain imaging was performed using CLARITY optimized lightsheet microscopy (COLM)[61], and 3D volume renderings were generated using Amira (FEI).

Quantitative morphometry of periventricular onecut-3$^+$ TH$^+$ neurons. Male *Dat1-Cre::B6.Cg-Gt(ROSA)26Sor$^{tm14(CAG-tdTomato)Hze}$*/J mice ($n = 6$) were deeply anesthetized with sodium pentobarbital and perfused with Tyrode's Ca^{2+}-free solution (10 ml, 37 °C) followed first by 10 ml 4% PFA and 0.2% picric acid (37 °C) and then by 50 ml of the same fixative at 4 °C. Brains were immersed in the same fixative for 90 min and cryoprotected in 15% sucrose in PBS (0.01 M, pH 7.4). Fourteen-micrometer-thick coronal sections were cut on a cryostat microtome and thaw-mounted onto glass slides. Sections rinsed in PBS were incubated with rabbit anti-TH (1:1,000; Millipore, cat. no. AB152) diluted in PBS containing 0.3% Triton X-100 at 4 °C for 16 h. After repeated rinses in PBS, sections were re-incubated with guinea pig anti-oncecut-3 antiserum[53] (1:1,250) at 4 °C for 16 h. Subsequently, tissues were simultaneously exposed to Alexa 488–conjugated goat-anti guinea pig and Alexa 647–conjugated goat anti-rabbit whole IgGs (Life Technologies, cat. no. A-11073 and A-21245, respectively). Sections were then washed for >30 min in PBS and mounted with ProLong Gold (Life Technologies). Photomicrographs were captured on a Zeiss LSM780 laser-scanning microscope. Three sections per animal, spaced at regular intervals across the periventricular region, were selected for quantification of fluorescently labeled neurons. The periventricular nucleus was divided into three levels according to Paxinos and Franklin[62]: rostral, bregma −0.22 mm (preoptic area); mid, bregma −0.58 mm (at suprachiasmatic nucleus); and caudal, bregma −0.94 mm (retrochiasmatic nucleus). Confocal micrograph montages of single optical sections covering the entire periventricular nucleus of each section were acquired with a 20× objective using an automatic stage controller. Occasionally, the brightness and contrast of the acquired images were adjusted. Cells in the periventricular region were counted manually offline using the merged as well as individual color channels. Only neurons situated ventral to the PVN and <120 µm from the lateral wall of the third ventricle were counted; neurons were counted in both hemispheres (**Fig. 5d** and **Supplementary Fig. 7d**).

Cell capture, imaging, lysis and RNA-seq. C57BL6/N juvenile mice (P14–28) of both sexes from control (untreated) and acutely stressed (formalin stress induced by injection of 4% PFA into the left paw)[18] experimental groups were used for cell collection. We used a 6-h time point because global changes in mRNA peak ~5–9 h after experimental manipulation[63]. The processing of cells from male and female animals was random to avoid any methodological bias. Mice were deeply anesthetized (5% isoflurane) and transcardially perfused with 40 ml ice-cold preoxygenated (95% O_2/5% CO_2) cutting solution containing (in mM) 90 NaCl, 26 $NaHCO_3$, 2.5 KCl, 1.2 NaH_2PO_4, 10 HEPES-NaOH, 5 sodium ascorbate, 5 sodium pyruvate, 0.5 $CaCl_2$, 8 $MgSO_4$ and 20 glucose. A central column of the mouse hypothalamus spanning the posterior preoptic area to the Arc (rostrocaudal axis), paraventricular nucleus (dorsal) and the ventrolateral hypothalamic area (lateral; **Fig. 1a**; see ref. 62) was microdissected from serial 300-µm-thick coronal slices under microscopy guidance and then dissociated using the Papain Dissociation System (Worthington). Isolated single cells were concentrated by centrifugation to a density of 600–1,000 cells/µl. After mixing C1 suspension reagent (4 µl; Fluidigm) with the cell suspension (7 µl), this mixture was loaded into a C1-AutoPrep IFC microfluidic chip designed for cells 10–17 µm in diameter (Fluidigm) and processed on a Fluidigm C1 instrument using the mRNA Seq: cell load (1772x/1773x) script (30 min at 4 °C). The microfluidic plate was then transferred to an automated microscope (Nikon TE2000E) to acquire a bright-field image of each capture site at 20× magnification using µManager (http://www.micro-manager.org/) in <15 min. Quality control for exclusion of debris or doublets was performed after each capture experiment. Following lysis, cDNA synthesis, amplification and tagmentation, high-throughput RNA sequencing was performed on an Illumina HiSeq2000 sequencer[9,64].

BackSpin algorithm. BackSpin is a biclustering algorithm that works in parallel on cells and genes. BackSpin is not based on dimensional reduction but on a series of binary splits, which allow focusing on the most relevant set of genes while clustering a subset of the cells. For each binary split, the points are sorted into one-dimensional order using the SPIN algorithm[65]. Here, we used BackSpinV2, which is a more adaptive and scalable version of the original algorithm[9], as shown by Marques *et al.*[66]. Conceptually, the V2 approach is identical to the BackSpin algorithm[9], with its full source code available at https://github.com/linnarsson-lab/BackSPIN/. The algorithm has by now been extensively validated using both computational (including comparisons to PCA, independent component analysis, tSNE, and GP-LVM) and biological validation tools[9,66–69].

Level 1 analysis. Data from all cells that passed visual quality control were imported as molecule counts (including all metadata annotations). Cells with more than 1,500 molecules/cell (excluding rRNA, mitochondrial RNA and repeats) were analyzed, resulting in a total of 3,131 cells. No statistical methods were used to predetermine sample sizes, but our sample sizes are similar to those reported for the cerebral cortex and hippocampus[9]. Genes with <50 molecules in the whole data set or expressed in >70% of the cells were excluded. Next, the BackSpinV2 algorithm was used with the following parameters: splitlev = 8; Nfeature = 500; N_to_backspin = 100; N_to_cells = 500; mean_tresh = 0.1; fdr_th = 0.2; min_gr_cells = 5; min_gr_genes = 2. Considering that our primary aim was to sort cells into molecularly defined clusters that correspond to main tissue and lineage subtypes, we manually inspected the borders of the ensuing clusters and merged clusters when thought necessary for the main cell types: oligodendrocytes, neurons, astrocytes, ependymal cells, endothelial cell, vascular lineage and microglia (**Fig. 1b**). **Figure 1c** shows a heat map with equal representation of genes that are specific to each of the main cell lineages: (i) oligodendrocytes (mRNAs for myelin basic protein (*Mbp*) and UDP glycosyltransferase-8 (*Ugt8*) involved in sphingolipid metabolism[70,71]); (ii) astrocytes (genes *Fabp7* and *Ntsr2*)[9,72]; (iii) ependymal cells (genes associated with motile cilia, including *Enkur*[9] and the transcription factor *Foxj1* (ref. 73)); (iv) microglia (mRNAs for macrophage lineage marker allograft inflammatory factor 1 (*Aif1*) and immunoglobulin E receptor (*Fcer1g*)[74]); (v) endothelial cells (genes encoding fibronectin (*Fn1*) and organic anion transporter (*Slco1a4*)[75]); (vi) vascular and smooth muscle lineage (mRNAs for the α2 subunit of actin (*Acta2*) and transgelin (*Tagln*)[76]); and (vii) neurons (genes *Ndrg4* and *Stmn2*)[9,18,77].

Level 2 analysis of neurons. This paper particularly addresses the diversity of hypothalamic neurons, and therefore neuronal clusters (**Fig. 1b**) were subjected to in-depth analysis. Data were from 898 cells that qualified as neurons based on level 1 clustering. To remove noise before clustering, we first used a primary (coarse) filter and selected for genes that were distinguished by *t*-test to be enriched in neurons using a false discovery rate (FDR) of 5% (results in 9,013 neuronal genes in total). BackSpinV2 was then used with the following parameters: splitlev = 7; Nfeture1 = 500; Nfeture = 200; N_to_backspin = 10; N_to_cells = 500; mean_tresh = 0.1; fdr_th = 0.3; min_gr_cells = 5; min_gr_genes = 3. This step distinguished 91 neuronal clusters (**Fig. 1c**). Next we manually removed putative artifactual clusters that had formed due to low or variable quality of RNA and then merged clusters that showed a high percentage of similarity; that is, none of the key markers differed between the two cell populations. Moreover, we

omitted clusters that appeared thalamus specific because of the presence of known thalamus-specific homeobox genes and transcription factors. These refinements led to 62 neuronal subclusters being discerned.

Selection of cluster-enriched genes and markers. For each gene *i* and cluster *j*, we followed the following mathematical formula:

$$\text{enrich}_{i,j} = \frac{1}{k \in j}\sum_{k \in j} E_{i,k} \Big/ \frac{1}{N}\sum_{k} E_{i,k}$$

$$\text{posfrac}_{i,j} = \frac{1}{k \in j}\sum_{k \in j} I(E_{i,k} > 0)$$

where $E_{i,k}$ is the expression of gene *i* in cell *k*. Quantities represent molecule enrichment in a specific cluster and in the fraction of cells that expressed the gene within that cluster. Next we combined the outcomes, weighed the fraction of positive cells and ranked the genes for each cluster by score: $S_{i,j} = \text{enrich}_{i,j} \times \text{posfrac}_{i,j}^{power}$, where *power* sets the weight for the fraction of positive cells in the cluster. We used *power* = 0, 0.5, 1 to rank genes in every cluster and then used the top *X* genes as most enriched. Specifically, the dendrogram in **Figure 2a** was built by using the top 5 genes per cluster. To identify new markers for each neuronal cluster (**Supplementary Fig. 6** and **Supplementary Tables 2** and **4**), we used *power* = 0.5 to identify the top hit in each cluster, excluding genes that were among the top 5 markers for any other cluster.

Dendrogram construction and split point listing. For generation of a dendrogram (**Fig. 2a**), we first selected genes enriched within the cluster so that each cluster was represented in a balanced way (that is, the top enriched genes within and selection of the top 5 from every *power* parameter; see above). This returned 401 genes, all of which, after a $\log_2 + 1$ transformation, was used to calculate the correlation between clusters. We used the Ward method to express correlation as distance for linkage to construct a hierarchical tree. To better understand the shape of the tree, we considered whether specific genes existed to explain each of the tree junctions. To this end, we used two independent criteria: the difference in the average and the difference in the fraction of positive (>0) cells (**Supplementary Table 3**). Thus, each junction defines a left and a right group by having the above score calculated at the single-cell level.

Error-bar plots. For the most comprehensive presentation of genes with meaningful expression over many clusters, we used the form of error-bar plots that show the means ± s.e.m. for each cluster. To construct relevant figures, we calculated the mean log expression for each gene in each cluster. First we normalized expression such that the total number of molecules (sum of all genes detected; **Supplementary Fig. 1c**) in every cell was set at 10,000. Next we transformed the results by $\log_2(x + 1)$ to calculate the means ± s.e.m. Likewise, we computed the fraction of positive cells per cluster. We present data in two forms: (i) with *power* = 0, where there is no correction for the fraction of positive cells and (ii) with *power* = 1, where the average is multiplied by the fraction of positive cells to avoid heterogeneous groups (cluster identity).

Calculating significance using the Wilcoxon rank-sum test. In this report, we use statistical analysis for the purpose of (i) declaring that particular gene *i* is expressed in group *j* significantly higher than the basal ('background') level and (ii) finding genes with hierarchical expression, for example, which differentiate junctions of the cluster dendrogram. To obtain levels of significance, we used the Wilcoxon rank-sum test, which is non-parametric and does not assume normality. We applied this test in a one-tailed fashion (using the MATLAB function 'ranksum' assuming that expression in the group tested is greater than in others). For the first case, the test is performed independently for each gene while sequentially analyzing the groups and testing each group against the rest of the cells. The process is subsequently repeated for each gene over the 62 groups, and for all genes. A similar process was carried out when testing dendrogram junctions. The *q* value was calculated as the *p* value corrected for multiple testing using horizontal correction across the 62 clusters with the Benjamini-Hochberg procedure[78] to control the false discovery rate (FDR). We consider gene expression significant if $q < 0.05$ (raw data for *p* and *q* values are shown in **Supplementary Tables 5** and **6**). To obtain the set of genes that distinguish any junction in the dendrogram (**Fig. 2a**), we tested each side of a particular junction against its other side using Wilcoxon's rank-sum test, corrected for multiple testing since each gene was tested for all 61 junctions. In addition, since in junction analysis genes that are exclusive (or almost exclusive) are of particular interest, we tested the number of cells with positive (greater than zero) expression using binomial distribution. Here, the *P* value is the binomial cumulative distribution function of *x*, *N* and *p*, where *x* is the number of positive cells, *N* is cluster size and *p* is the fraction of positive cells in both groups. These results are shown in **Supplementary Table 3** with the top genes relevant to differentiate each junction.

Statistical analysis of histochemical and imaging data. None of the experiments required data collection in a blinded fashion. Data were analyzed using SigmaPlot (Systat Software Inc.). Data were expressed as means ± s.e.m. A *P*-value of < 0.05 was considered statistically significant and calculated using Student's *t*-test (on independent samples), one-way analysis of variance (ANOVA with Dunn's *post hoc* test) or Mann-Whitney's *U*-test as appropriate. The non-parametric Kolmogorov-Smirnov test was used for the determination of diurnal variations in phospho-TH levels.

tSNE projections. We used *t*-distributed stochastic neighbor embedding (tSNE)[79] to visualize neuronal complexity in two dimensions (no effect on clustering). To present single-cell RNA-sequencing data, which is naturally of high dimensions, one needs to choose a dimensional reduction method that is either linear (principal component analysis) or nonlinear (tSNE). We chose tSNE because many single-cell RNA-sequencing studies show this to be the most powerful in keeping multiple structures within the data sets[9,67,68]. tSNE projections (**Fig. 1d**) were calculated on neuronal data after selecting 1,194 cluster-enriched genes as used for dendrogram construction (see above). We used 200 principal components; perplexity = 5, 10 or 20, ε (initial learning rate) = 100 and correlation as a distance measure.

Drop-seq. Drop-seq was performed as previously published[22]. Briefly, single-cell suspensions were prepared in PBS containing BSA at a concentration of 30,000 cells/ml. Barcoded beads (Chemgenes) were resuspended in lysis buffer containing DTT at a concentration of 100,000 beads/ml. Syringes containing oil, beads and cell suspension were connected to a Drop-seq microfluidics chip (FlowJEM), and individual flow rates were adjusted to achieve constant and productive flow. Droplets were collected in a 50 ml Falcon tube. Excess oil at the bottom of the tube below the droplet-containing phase was removed. Droplet breakage, subsequent reverse transcription and exonuclease treatment were conducted as described[22]. cDNA was PCR amplified by 4 initial cycles at 65 °C followed by 12 cycles at 67 °C annealing temperature. cDNAs were fragmented and amplified with the Nextera XT DNA sample prep kit (Illumina) using custom primers that enabled the specific amplification of only their 3′ ends. cDNA and library concentrations were assessed using the Qubit dsDNA HS assay (Life Technologies), and fragment distribution was determined using high-sensitivity DNA chips on a 2100 Bioanalyzer (Agilent). Sequencing was performed using the 75-bp paired-end configuration on an Illumina HiSeq 3000/4000 platform.

Drop-seq analysis. Drop-seq data processing of 220 neurons as output was performed using the Drop-seq Tools v1.12 software[22]. Briefly, each transcriptome Read 2 was tagged with the cell barcode (bases 1 to 12) and UMI barcode (bases 13 to 20) obtained from Read 1, trimmed for sequencing adapters and poly(A) sequences and aligned to the mouse genome (Ensembl GRCm38 release) using STAR v2.4.0 (ref. 80). Reads aligning to exons were tagged with the respective gene name, and counts of unique UMIs per gene in each cell were used to build a digital gene expression matrix. Read counts for each gene were posteriorly normalized to the total coverage per cell.

Ca^{2+} imaging. Coronal hypothalamic slices containing the periventricular and Arc nuclei were prepared from male *Th-GFP* mice (2–4 weeks old). In brief, mice were deeply anesthetized (5% isoflurane) and brains were rapidly removed and immersed in ice-cold preoxygenated (95% O_2/5% CO_2) cutting solution containing (in mM) 90 NaCl, 26 $NaHCO_3$, 2.5 KCl, 1.2 NaH_2PO_4, 10 HEPES-NaOH, 5 sodium ascorbate, 5 sodium pyruvate, 0.5 $CaCl_2$, 8 $MgSO_4$ and 20 glucose. Subsequently, 250-µm-thick coronal slices were cut on a vibratome (VT1200S, Leica). Slices encompassing the periventricular nucleus were selected and equilibrated in artificial cerebrospinal fluid (ACSF) containing (in mM) 124 NaCl,

doi:10.1038/nn.4462

26 $NaHCO_3$, 2.5 KCl, 1.2 NaH_2PO_4, 2 $CaCl_2$ and 2 $MgSO_4$ at 22–24 °C for 1–4 h before recording. Before imaging, slices were transferred into ACSF containing 10–20 µM FURA2-AM for 40–90 min (loading). Recordings were done using a VisiChrome monochromator and VisiView software (Visitron Systems) on an AxioExaminer.D1 microscope (Zeiss) equipped with a CoolSnap HQ^2 camera (Photometrics). Neuromedin S was from Tocris; 55 mM KCl solution contained (in mM) 71.5 NaCl, 26 $NaHCO_3$, 55 KCl, 1.2 NaH_2PO_4, 2 $CaCl_2$ and 2 $MgSO_4$.

Human, tissue preparation and histochemistry. We applied direct perfusion via the internal carotid and vertebral arteries, which facilitated the preservation of tissue integrity relative to alternative fixation methods. Human brains ($n = 2$, gender and age: female 83 years and male 79 years, ethical approval: TUKEB 84/2014, Hungary) were first perfused with physiological saline followed by a fixative containing 2% PFA and 0.1% glutaraldehyde in 0.1 M Tris-buffered saline (TBS, pH 7.4) 7 h or 11 h after death. The removal and subsequent preparation of human tissues were in accordance with ethical guidelines of Semmelweis University (1998, Budapest, Hungary). Hypothalami were dissected out and post-fixed in 2% PFA in TBS for 72 h, followed by immersion in cryoprotective 30% sucrose in 0.1 M PB (pH 7.4) overnight. Coronal sections (50 µm) were cut on a cryostat microtome and processed for immunohistochemistry. Free-floating sections were rinsed in PB (pH 7.4) and pretreated with 0.3% Triton-X 100 (in PB) for 1 h at 22–24 °C to enhance the penetration of antibodies. Nonspecific immunoreactivity was suppressed by incubating specimens in a cocktail of 5% NDS (Jackson), 10% BSA (Sigma) and 0.3% Triton X-100 (Sigma) in PB for 1 h at 22–24 °C. Sections were exposed for up to 72 h (at 4 °C) to the following mixture of primary antibodies diluted in PB to which 0.1% NDS and 0.3% Triton X-100 had been added: guinea pig anti-onecut-3 (1:5.000)[53], mouse anti-TH (Millipore, 1:500, cat. no. MAB5280), rabbit anti-phospho-Ser40-TH (Millipore, 1:500, cat. no. AB5935). After extensive rinsing in PB, immunoreactivities were revealed by Cy2-, Cy3- or Cy5-tagged secondary antibodies raised in donkey (1:200, Jackson, cat. nos. as above; 2 h at 22–24 °C). Lipofuscin autofluorescence was quenched by applying Sudan black B (1%, dissolved in 70% ethanol[81]). Glass-mounted sections were coverslipped with Aquamount embedding medium (Dako). Sections were inspected and images acquired on a 710LSM confocal laser-scanning microscope (Zeiss) at 10× or 40× primary magnification, and pinhole settings limiting signal detection to 0.5–0.7 µm. Emission spectra for each dye were limited as follows: Cy2, 505–530 nm; Cy3, 560–610 nm; Cy5, 650–720 nm. Multi-panel figures were assembled in CorelDraw X7 (Corel Corp.).

***In situ* hybridization.** In accord with applicable publication policies, images presented here are from publicly available resources of the Allen Brain Atlas. Particularly, images are from the Adult Mouse Atlas resource with experiments 75041585, 74882808, 79591637, 77371835, 793, 79591365 for the genes *Qrfp*, *Npvf*, *Grp*, *Vip*, *Per2* and *Slc6a3*, respectively (http://www.alleninstitute.org/).

Data availability. Sequence data have been deposited in Gene Expression Omnibus, accession code GSE74672. For each gene, data can be analyzed and visualized online at http://linnarssonlab.org/hypothalamus/. All other data that support the findings of this study are available from T. Harkany upon reasonable request.

All supplementary information and source data are available in the online version of the paper and at http://linnarssonlab.org/hypothalamus/.

A **Supplementary Methods Checklist** is available.

51. Tamamaki, N. *et al.* Green fluorescent protein expression and colocalization with calretinin, parvalbumin, and somatostatin in the GAD67-GFP knock-in mouse. *J. Comp. Neurol.* **467**, 60–79 (2003).
52. Máté, Z. *et al.* Spatiotemporal expression pattern of DsRedT3/CCK gene construct during postnatal development of myenteric plexus in transgenic mice. *Cell Tissue Res.* **352**, 199–206 (2013).
53. Pierreux, C.E., Vanhorenbeeck, V., Jacquemin, P., Lemaigre, F.P. & Rousseau, G.G. The transcription factor hepatocyte nuclear factor-6/Onecut-1 controls the expression of its paralog Onecut-3 in developing mouse endoderm. *J. Biol. Chem.* **279**, 51298–51304 (2004).
54. Wong, H.C., Sternini, C., Lloyd, K., De Giorgio, R. & Walsh, J.H. Monoclonal antibody to VIP: production, characterization, immunoneutralizing activity, and usefulness in cytochemical staining. *Hybridoma* **15**, 133–139 (1996).
55. Miyazaki, T., Fukaya, M., Shimizu, H. & Watanabe, M. Subtype switching of vesicular glutamate transporters at parallel fibre-Purkinje cell synapses in developing mouse cerebellum. *The European journal of neuroscience* **17**, 2563–2572 (2003).
56. Mulder, J. *et al.* Secretagogin is a Ca2+-binding protein identifying prospective extended amygdala neurons in the developing mammalian telencephalon. *Eur. J. Neurosci.* **31**, 2166–2177 (2010).
57. Weiss, M.L. & Cobbett, P. Intravenous injection of Evans blue labels magnocellular neuroendocrine cells of the rat supraoptic nucleus in situ and after dissociation. *Neuroscience* **48**, 383–395 (1992).
58. Murray, A.J. *et al.* Parvalbumin-positive CA1 interneurons are required for spatial working but not for reference memory. *Nat. Neurosci.* **14**, 297–299 (2011).
59. Pollak Dorocic, I. *et al.* A whole-brain atlas of inputs to serotonergic neurons of the dorsal and median raphe nuclei. *Neuron* **83**, 663–678 (2014).
60. Susaki, E.A. *et al.* Whole-brain imaging with single-cell resolution using chemical cocktails and computational analysis. *Cell* **157**, 726–739 (2014).
61. Paxinos, G. & Franklin, K.B.J. *The Mouse Brain in Stereotaxic Coordinates* (Academic, San Diego, 2001).
62. Tomer, R., Ye, L., Hsueh, B. & Deisseroth, K. Advanced CLARITY for rapid and high-resolution imaging of intact tissues. *Nat. Protoc.* **9**, 1682–1697 (2014).
63. Schwanhäusser, B. *et al.* Global quantification of mammalian gene expression control. *Nature* **473**, 337–342 (2011).
64. Islam, S. *et al.* Quantitative single-cell RNA-seq with unique molecular identifiers. *Nat. Methods* **11**, 163–166 (2014).
65. Tsafrir, D. *et al.* Sorting points into neighborhoods (SPIN): data analysis and visualization by ordering distance matrices. *Bioinformatics* **21**, 2301–2308 (2005).
66. Marques, S. *et al.* Oligodendrocyte heterogeneity in the mouse juvenile and adult central nervous system. *Science* **352**, 1326–1329 (2016).
67. Fan, J. *et al.* Characterizing transcriptional heterogeneity through pathway and gene set overdispersion analysis. *Nat. Methods* **13**, 241–244 (2016).
68. Tasic, B. *et al.* Adult mouse cortical cell taxonomy revealed by single cell transcriptomics. *Nat. Neurosci.* **19**, 335–346 (2016).
69. Fuzik, J. *et al.* Integration of electrophysiological recordings with single-cell RNA-seq data identifies neuronal subtypes. *Nat. Biotechnol.* **34**, 175–183 (2016).
70. Sprong, H. *et al.* UDP-galactose:ceramide galactosyltransferase is a class I integral membrane protein of the endoplasmic reticulum. *J. Biol. Chem.* **273**, 25880–25888 (1998).
71. Jahn, O., Tenzer, S. & Werner, H.B. Myelin proteomics: molecular anatomy of an insulating sheath. *Mol. Neurobiol.* **40**, 55–72 (2009).
72. Ebrahimi, M. *et al.* Astrocyte-expressed FABP7 regulates dendritic morphology and excitatory synaptic function of cortical neurons. *Glia* **64**, 48–62 (2016).
73. Roy, S. The motile cilium in development and disease: emerging new insights. *Bioessays* **31**, 694–699 (2009).
74. Liu, G., Ma, H., Jiang, L. & Zhao, Y. Allograft inflammatory factor-1 and its immune regulation. *Autoimmunity* **40**, 95–102 (2007).
75. Ose, A. *et al.* Functional characterization of mouse organic anion transporting peptide 1a4 in the uptake and efflux of drugs across the blood-brain barrier. *Drug Metab. Dispos.* **38**, 168–176 (2010).
76. Li, L., Miano, J.M., Cserjesi, P. & Olson, E.N. SM22 alpha, a marker of adult smooth muscle, is expressed in multiple myogenic lineages during embryogenesis. *Circ. Res.* **78**, 188–195 (1996).
77. Tortoriello, G. *et al.* Miswiring the brain: Δ^9-tetrahydrocannabinol disrupts cortical development by inducing an SCG10/stathmin-2 degradation pathway. *EMBO J.* **33**, 668–685 (2014).
78. Benjamini, Y. & Hochberg, Y. Controlling the false discovery rate – a practical and powerful approach to multiple testing. *J. R. Stat. Soc. Series B Stat. Methodol.* **57**, 289–300 (1995).
79. van der Maaten, L. & Hinton, G. Visualizing data using t-SNE. *J. Mach. Learn. Res.* **9**, 2579–2605 (2008).
80. Dobin, A. *et al.* STAR: ultrafast universal RNA-seq aligner. *Bioinformatics* **29**, 15–21 (2013).
81. Schnell, S.A., Staines, W.A. & Wessendorf, M.W. Reduction of lipofuscin-like autofluorescence in fluorescently labeled tissue. *J. Histochem. Cytochem.* **47**, 719–730 (1999).